Benjamin Kain, BSc.

Investigation of Antimony Perovskite Materials as Potential Absorber Material in Solar Cells

Master thesis

In partial fulfillment of the requirements for the academic degree

Diplom-Ingenieur

in the field of study of Technical Chemistry

Submitted to

Graz University of Technology

Supervisor

Assoc. Prof. Dipl.-Ing. Dr. techn. Gregor Trimmel

Institute for Chemistry and Technology of Materials

Graz, October 2017

EIDESSTATTLICHE ERKLÄRUNG

Ich erkläre an Eides statt, dass ich die vorliegende Arbeit selbstständig verfasst, andere als die angegebenen Quellen/Hilfsmittel nicht benutzt, und die den benutzten Quellen wörtlich und inhaltlich entnommenen Stellen als solche kenntlich gemacht habe. Das in TUGRAZonline hochgeladene Textdokument ist mit der vorliegenden Masterarbeit identisch.

AFFIDAVIT

I declare that I have authored this thesis independently, that I have not used other than the declared sources/resources, and that I have explicitly indicated all material which has been quoted either literally or by content from the sources used. The text document uploaded to TUGRAZonline is identical to the present master's thesis.

_____ _____

Date Signature

Abstract

In the field of photovoltaic solar cells, perovskite solar cells are an emerging technology due to their fast development and increase of the power conversion efficiency over the past years. Mainly lead-based perovskite absorber materials are accountable for the high interest in this technology. Due to the toxicity and the environmental harmfulness of lead, alternative potential lead-free perovskite materials were investigated. In the last few years, tin and germanium perovskites were investigated as they seem to be the first choice due to the similar electronic configuration and being in the same group of the periodic table. In this master thesis, approaches for trivalent substitution of the lead (Pb^{2+}) ion with the antimony (Sb^{3+}) ion were made. Different materials such as rubidium antimony iodide ($Rb_3Sb_2I_9$) and methyl ammonium antimony iodide ($MA_3Sb_2I_9$) were characterized via X-ray diffractometry to gain information about the crystal structure and the crystal orientation in the material. UV/VIS spectra were recorded to obtain optical properties of the material. The absorption coefficient and the bandgap as well as the Urbach energy were determined, which provides information about the impurities and disorders in the material. Furthermore, I/V curves were measured to investigate the photovoltaic properties of the materials. In the ABX_3 structure the influence of different anion ratios of bromide and iodide was observed and characterized. Furthermore, the external quantum efficiency and photoluminescence spectra were measured. During this thesis, solar cell devices were fabricated in two different setups; a TiO_2 based device setup with an architecture as followed: glass/ITO/compact-TiO_2/mesoporous-TiO_2/Perovskite/Spiro-MeOTAD/Ag. The TiO_2 layers act as an electron-transport material (ETM), spiro-MeOTAD as a hole-transport material (HTM) and ITO and silver as electrodes. in the second architecture solar cells in an inverse setup were fabricated as followed: glass/ITO/PEDOT:PSS/Perovskite/$PC_{70}BM$/Ag, where PEDOT:PSS acts as HTM and $PC_{70}BM$ as ETM. Using different device setups make it possible to further investigate the interaction between the perovskite and different ETM and HTM respectively. Finally, comparing the results with the literature the fabricated solar cells are not only competing with existing Sb-based perovskite solar cells but exceeding in terms of efficiency.

Kurzfassung

Perowskit-Solarzellen sind eine neuartige Technologie, welche, aufgrund der raschen Effizienzsteigerung von bleihaltigen Perowskit-solarzellen, in den letzten Jahren großes Interesse geweckt hat. Da Blei nicht nur für die Menschen giftig, sondern auch für die Umwelt schädlich ist, werden bleifreie Alternativen erforscht. Zu Beginn wurden Zinn- und Germanium-Perowskite aufgrund ihrer ähnlichen Elektronenkonfiguration untersucht. Dieser Umstand lässt auch vermuten, dass diese ähnliche Eigenschaften wie Blei Perowskite aufweisen. Thema dieser Arbeit ist der Versuch das zweiwertige Bleikation mit einem dreiwertigen Antimonkation in der Perowskitstruktur zu ersetzen. Verschiedene Materialien wie Rubidiumantimoniodid ($Rb_3Sb_2I_9$) und Methylammoniumantimoniodid ($MA_3Sb_2I_9$) wurden durch Aufnahme ihrer UV/VIS Spektren auf ihre optischen Eigenschaften untersucht und der Absorptionskoeffizient, die Bandlücke sowie die Urbach Energie wurden daraus berechnet. Mittels Röntgendiffraktometrie wurde die Kristallstruktur sowie deren Orientierung im Material bestimmt. Die Hauptaufgabe in dieser Arbeit war es verschiedene Sb-haltige Materialien zu untersuchen und Solarzellen anzufertigen, um möglichst gute Effizienzen zu erzielen, welche über ihre Strom-Spannungs-Kennlinie bestimmt wurden. Weiters wurde Iodid teilweise mit Bromid in der Kristallstruktur $A_3B_2X_9$ ersetzt und der Einfluss mittels externen Quantenausbeute- und Photolumineszenz-Messungen untersucht und charakterisiert. Solarzellen wurden in zwei verschiedenen Aufbauten hergestellt, um den Einfluss zwischen der Perowskitschicht und der angrenzenden Elektronentransportschicht (ETM) und Lochtransportschicht (HTM) zu untersuchen. Nachfolgend ist das Setup auf Basis von TiO_2 dargestellt: Glass/ITO/kompakte-TiO_2/mesoporöse-TiO_2/Perowskit/Spiro-MeOTAD/Ag. Die zwei TiO_2-Schichten agieren hierbei als ETM und Spiro-MeOTAD als HTL. Silber und ITO wirken als Elektroden. Das zweite Setup wurde auf PEDOT:PSS wie folgt hergestellt: Glas/ITO/PEDOT:PSS/Perowskit/$PC_{70}BM$/Ag. Hier wirkt PEDOT:PSS als HTL und $PC_{70}BM$ als ETL. Zu guter Letzt wurden die Ergebnisse zusammengefasst und mit bestehender Literatur verglichen. Dabei stellte sich heraus, dass die hergestellten Solarzellen nicht nur vergleichbar gute Effizienzen aufweisen, sondern diese übertreffen.

Acknowledgements

I would like to thank my supervisor Assoc. Prof. Dipl.-Ing. Dr. techn. Gregor Trimmel for giving me the opportunity to work in the field of renewable resources and perform my master thesis under his charge. Furthermore, I want to thank the project “Permasol”.

I especially want to thank Dr. Thomas Rath, Dipl.-Ing. Sebastian Höfler and Bastian Friesenbichler BSc. for their input, ideas and helpful discussions. Moreover, I would like to thank the whole working group for the great time I had and for being part of the team.

A special thanks goes to Birgit Kunert for the X-ray diffraction measurements.

My deepest gratitude goes to my family, especially my parents, who supported me during the whole course of my studies. This would not have been possible without you.

List of Abbreviations

BCP	bathocuproine
CIGS	copper indium gallium selenide
DMF	dimethylformamide
DSSC	dye-sensitized solar cell
EQE	external quantum efficiency
ETL	electron transport layer
ETM	electron transport material
FA	foramamidinium
FF	fill factor
FK-209	tris(2-(1*H*-pyrazol-1-yl)-4-*tert*-butylpyridine)cobalt(III)-tri[bis(trifluoromethane)-sulfonimide]
HOMO	highest occupied molecular orbital
HTL	hole transport layer
HTM	hole transport material
ITO	indium doped tin oxide
JSC	short circuit current density
Li-TFSi	bis(trifluoromethane)sulfonimide lithium salt
LUMO	lowest unoccupied molecular orbital
MA	methyl ammonium
MPP	maximum power point
NP	nanoparticle
PC60BM	[6,6]-Phenyl C61 butyric acid methyl ester

PC70BM	[6,6]-Phenyl C71 butyric acid methyl ester
PCE	power conversion efficiency
PEDOT:PSS	poly(3,4-ethylenedioxythiophene) polystyrene sulphonate
PV	photovoltaic
Spiro-MeOTAD	2,2´,7,7´-tetrakis(N,N-pdimethoxyphenylamino)-9,9´-spirobifluorene
TBP	4-*tert*-butylpyridine
VOC	open circuit Voltage
XRD	X-Ray diffraction

Table of Contents

1. Introduction:

1.1. Worldwide energy demand

The energy consumption worldwide and therefore the energy demand is rising ever since. Nowadays and in the near future, the demand increases primarily caused by developing countries with strong economic growth and expanding population. For these countries, an energy demand rise of over 70% from 2012 to 2040 is expected. the world energy consumption is influenced by the economic growth and improved living standards. Alongside the recent accessibility of electricity for parts of the population, their improved housing leading to a higher demand of energy due to construction and to maintain, as well as new transportation equipment and appliances for the new living standard are main reasons of the fast growth of the energy demand[1].

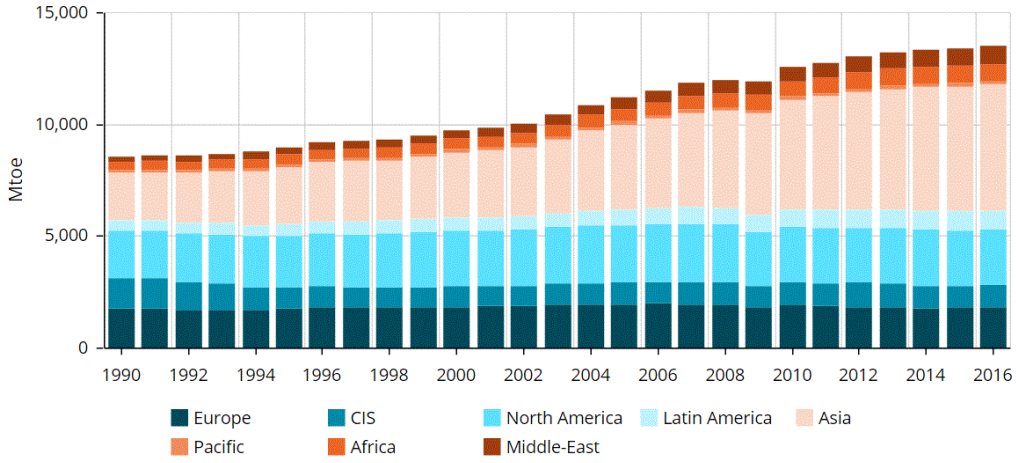

Figure 1: world energy demand since 1990, reprinted from yearbook.Enerdata.net[2]

The worldwide energy demand visualized in Figure 1 shows the increase of demand especially for continents with developing countries over 26 years given in Mtoe (million tons of oil equivalent). These days about 13 % of the energy production comes from renewable resources[2]. To obtain an ongoing increase of renewable resources, economic viability must be given and therefore successive research in that field must be maintained.

1.2. Renewable resource: solar energy

Solar energy was used throughout the history of mankind. This energy source was first used by ancient civilizations by drying food to preserve them. History shows, that already 200 years B.C. Archimedes used concentrated sunlight to set ships on fire from a distance. If this concentration was achieved by reflecting mirrors or by reflecting shields from soldiers arranged in a parabola, is unclear. Whether a myth or not, until now mankind was fascinated by the suns power and its possible application since then[3].

The first documented application was a solar furnace in 1774. Up to 1750 °C could be achieved by arranging a lens as a collector and a second smaller one to obtain such temperature. During the nineteenth century attempts of converting solar energy into another form were made based upon the generation of low pressure steam engines. Up to today, many large solar plants produce electricity by concentrating solar rays and transform it into superheated steam which is then converted to electricity by running steam engines.

In 1839 the photovoltaic effect was first discovered in selenium by Edmond Becquerel. Over a century later, the conversion efficiency reached a height of 11 % by using silicon. This photovoltaic cell found its first application in space because solar energy was the only power source available out there. By then research for alternative photovoltaic materials was rising. Crystalline silicon wafers with thickness of up to 300 µm are commonly used. Further investigations result in the development of an amorphous thin layer silicon solar cell. Even though the efficiency is lower compared to crystal ones, it has several advantages in terms of good light absorption, flexibility, low thickness of around 1 µm, easy and cheap processability. All these advantages result in low cost solar cells[5].

Due to this discovery, research for alternative thin layer solar cells like dye sensitized-, organic-, and perovskite-based solar cells emerged.[4]

1.3. Aim of this thesis

The aim of this thesis is the investigation of lead-free perovskite solar cells, using the trivalent antimony as B cation instead the commonly used divalent lead cation. Because antimony is a trivalent substitute, the crystal structure ABX_3 changes to $A_3B_2X_9$, where A is a monovalent cation, B a divalent or a trivalent cation, respectively, and X a monovalent anion.

Antimony perovskites were investigated as absorber materials using different characterization methods such as UV/VIS spectroscopy to determine the absorption as well as the bandgap of the material. The surface for possible pinhole formations was observed via an optical microscope. The performance of fabricated solar cells was determined by current-voltage characteristics. Moreover, using EQE (external quantum efficiency) the light conversion from photons into a current at different incident light wavelengths was determined.

The following chapter 2 deals with the basics of solar cells and their principles, a brief introduction to alternative non-silicon based solar cells and state of the art perovskite solar cells.

Chapter 3 describes the experimental work which was done during this thesis, where different device setups for solar cell preparation are described, whilst in chapter 4 the achieved results are presented and discussed, finishing the work with a conclusion thereafter.

2. Theoretical Background:

2.1. Basics of photovoltaic systems

Photovoltaic (PV) modules convert sunlight directly into electricity without any transition state such as heated steam powering engines. These PV-modules do not have moving parts and are solid state devices, resulting in a long lifetime and minimal maintenance. It is categorized as a renewable resource generator not producing any emission of greenhouse gases or any others while operating silent[5], but when being produced.

2.1.1. Photovoltaic effect and the electron band structure

Every electron possesses a specific quantized energy level. This energy level is dependent on the orbital and therefore dependent on the averaged distance to the positively charged nucleus. Innermost electrons have a minimum of energy and therefore require a relatively large amount of energy to overcome the attraction of its nucleus. Bringing atoms close together the energy of atoms is altered and the energy level forming energy bands. Only the outermost electrons are able to interact with other atoms and forming the highest normal filled band, the so-called valence band. In the valence band electrons are loosely attached to the nucleus with a high potential to charge another atom negatively and leaving a positively charged nucleus behind. Electrons with a lot of energy are able to jump from this valence band to the conduction band which is responsible for the conduction of electricity. The energetic difference of these two bands is the bandgap. This bandgap provides information about the energy needed for an electron to jump from the valence band to the conduction band[5].

The energy of this bandgap divides all materials in three categories depending on this energy level; a conductor, a semiconductor and an insulator. In a conductor, the valence band and conduction band are overlapping making it possible for electrons to fill the conduction band and accept energy from external fields. Semiconductors have bandgaps below 3 eV and have the same band structure as insulators. For electrons to overcome the bandgap electrons need to be excited; in photovoltaic solar cells in form of absorption of photons. Insulators have a bandgap of over 3 eV and are therefore not suitable for electron transfer[6].

Following Figure 3 shows a scheme of the energy band for these three types of materials.

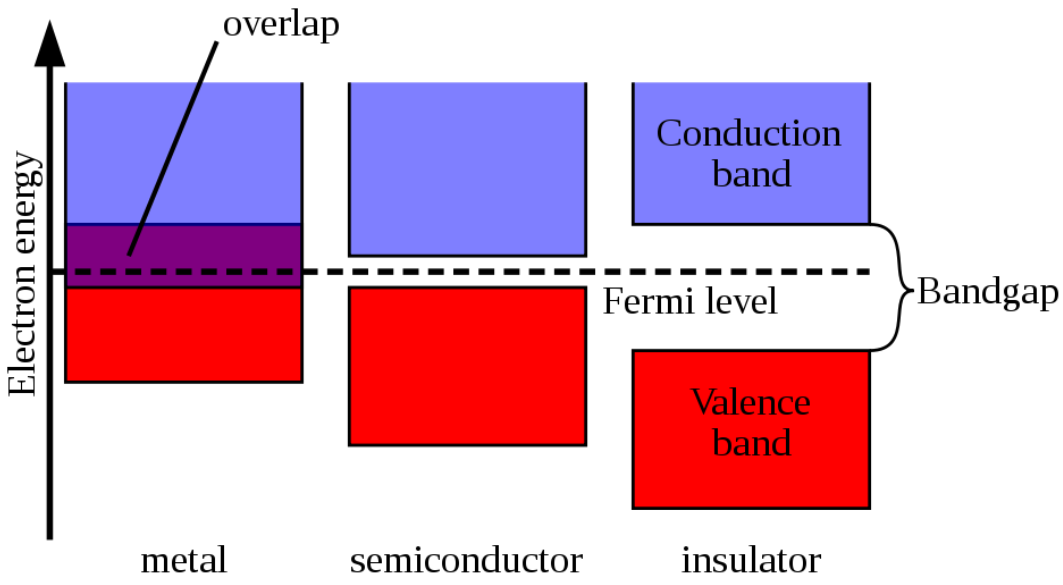

Figure 2: Band gap diagram of a conductor, a semiconductor, and an insulator

As depicted, a semiconductor is only conducting when an electron can jump across the forbidden zone from the valence band, which is the ground state of the electron, to the conduction band, which refers to an excited state of an electron. If a photon does not provide the amount of energy needed to overcome the bandgap, it will not be absorbed and transmission occurs.

A photovoltaic active material can be understood as a material able to absorb photons and creating a current. A photon hits an electron in the valence band and transfers its complete energy to the electron. Due to this excitation, the electron can then jump from the valence band which corresponds to the HOMO (highest occupied molecule orbital) in organic semiconductors to the conduction band which refers to the LUMO (lowest unoccupied molecule orbital) in organic semiconductors, if the energy of the photon is sufficient.

The energy of a photon is only dependent from its wavelength, due to the absence of mass and can be calculated by following Equation 1[5].

$$E_P = h\frac{C}{\lambda}$$

Equation 1: calculation of the energy of a photon

E_P = energy of the photon (J), h = Planck's constant (Js),
C = speed of light (ms^{-1}) and λ = wavelength (m)

After having an electron loosed from its atom, an electric field can remove the electron across the front or back of the material to generate a current. In the absence of an electric field the electron will recombine with the hole in a non-radiative recombination creating no current or radiative recombination with light emission of photons, instead of producing a current.

It needs to be kept in mind that no matter how high the photons energy is, for most photovoltaic systems only one electron can be freed from its atom making these photovoltaic materials limited in terms of efficiency. An exception hereby are the so called quantum dot solar cells.

2.1.2. Electrical characteristics of solar cells

Recording a current/voltage curve (I/V) the electrical characteristics of a solar cell is determined. Typically, the current is measured by varying the voltage of the cell through an applied load. Measuring the cell in illuminated and in dark condition both provide different data and information about the cell. Plotting the data shows the photodiodic behavior of the solar cell[7].

To compare solar cells with each other, the light source is standardized[8] matching the power output to 100 mW/cm^2.

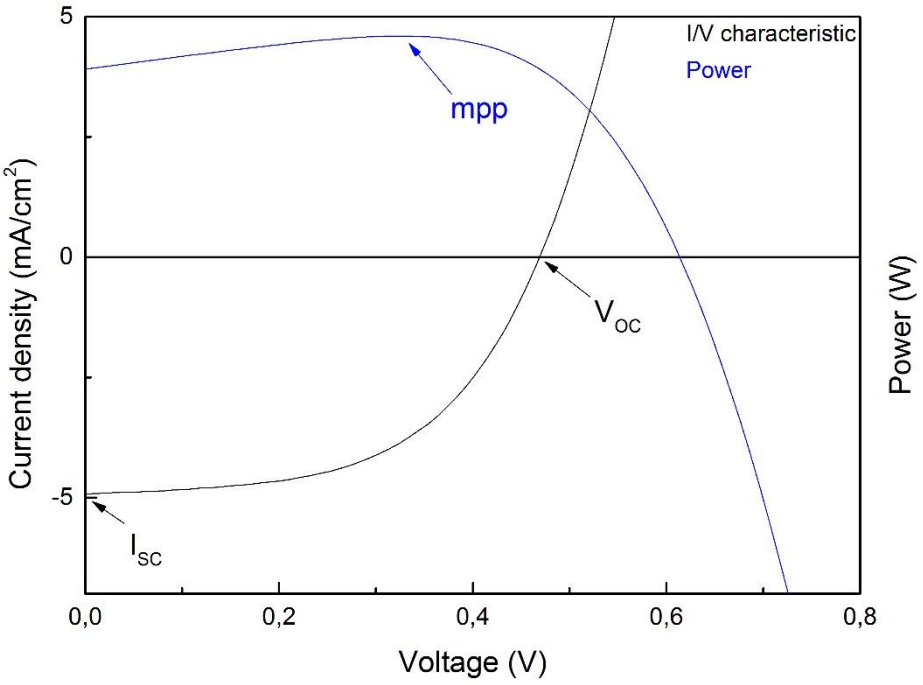

Figure 3: illustration of a typical I/V curve

The I_{SC}, or short circuit current, is the maximum current that can be retrieved with zero voltage across the cell. This is comparable to connected positive and negative leads. The I_{SC} is influenced by charge separation as well as transport efficiency of the device, the area of the solar cell as well as the incident light intensity and photon harvesting

On the other extreme, the open circuit voltage (V_{OC}) is the maximum potential of the cell while the current is zero. It represents the maximum voltage that can be achieved between the two electrodes. The V_{OC} is located where the internal voltage of the device is compensated by the applied voltage. The V_{OC} depends on the bandgap energy as well as on the interface with the ETL and HTL by HOMO/LUMO energy level differences and of the materials morphology[9].

In either point the power (current × voltage) is zero. The maximum power point (mpp) of a solar cell is located where the product of the voltage and the current reaches its maximum[10].

The fill factor (FF) is defined as the ratio of the mpp and the product of V_{OC} and I_{SC}. It describes the quality of the diode in an I/V curve. The quality depends on the serial resistance contact of the electrodes and for some materials on the morphology of the active layer[11].

$$FF = {}^{mpp}/_{I_{SC} \times V_{OC}}$$

Equation 2: FILL Factor calculation

The power conversion efficiency (PCE) provides information of the conversion of absorbed light into electrical power. Therefore, it is calculated by the ratio of mpp and the power input, which is, as discussed, already standardized to 100 mW/cm^2.

$$PCE = {}^{P_{out}}/_{P_{in}} = \frac{mpp}{P_{in}} = \frac{I_{SC} \times V_{OC} \times FF}{P_{in}}$$

Equation 3:power conversion efficiency

The external quantum efficiency (EQE) for a solar cell represents the efficiency of absorbing incident photons and converting them into electric power in regard of their wavelength. This can be divided into five substeps, represented by absorption efficiency η_{abs}, dissociation efficiency η_{diss}, diffusion efficiency η_{diff}, charge carrier transport efficiency η_{tr} and charge collection efficiency efficiency η_{cc}, respectively.

$$EQE = \frac{1240 \times I_{SC}}{\lambda \times P_{in}} = \eta_{abs} \times \eta_{diss} \times \eta_{diff} \times \eta_{tr} \times \eta_{cc}$$

Equation 4: external quantum efficiency

2.2. Alternative thin layer solar cells

As an alternative to silicon based solar cells, cadmium telluride gained lot recognition as a thin film solar cell material. With an optical bandgap of 1.5 eV, it matches the solar spectrum for photovoltaic conversion optimal. With its high absorption coefficient of over 5 $\times 10^5$ cm^{-1} nearly all photons, according to the absorption spectra, are absorbed in a 2 µm CdTe film[12]. This makes cadmium telluride solar cells thinner in regard to crystalline silicon solar cell by a factor of 100. Due to large development by a single manufacturer a low cost solar cell module(< 1 $ per watt) with an efficiency of around 11 % was achieved in combination with a large production capacity[5], making them commercial available. A high efficiency of 22.1 % was achieved already in the laboratory[13].

With an efficiency record of 22.6 %[14] copper indium gallium selenide (CIGS) solar cells are another promising alternative solar cell technology. Commercial available CIGS modules have efficiencies of around 13-15 %, making them one of the most efficient thin film solar cells. Like other thin film solar cells, it can be manufactured at low cost and lightweight. In combination with its flexibility, CIGS are a main candidate for commercial development without using glass as substrate. These properties making it ideal for residential as well as commercial rooftop installations and for building integrated photovoltaic products[5].

Another alternative to silicon based photovoltaic devices are dye sensitized solar cells (DSSC) due to its advantages of competitive prices, clean materials, an easy fabrication process and an efficiency of around 12 %[15]. In DSSCs, a photo sensitizer located on the TiO_2 surface absorbs an incident photon and getting in an excited state. The electron jumps into the TiO_2 conduction band and is conducted away through the external circuit. The therefore oxidized photosensitizer then accepts electrons from the redox mediator reduces it to the ground state. The oxidized redox mediator diffuses towards the counter electrode accepting the electron which was conducted through an external circuit and is therefore reduced again[16].

There are also other solar cells such as multi junction solar cell, organic solar cells as well as quantum dot solar cell, which are currently under development.

2.3. Perovskites as photovoltaic active material in solar cells

The origin of perovskite comes from the calcium titanium oxide mineral first found in 1839 by Gustav Rose and is named after the Russian mineralogist Lev Perovski. The name lends to a class of crystal structure with the type of $A^{1+}B^{2+}X^{1-}{}_3$, where A and B are cations differing greatly in their size and X is an anion. Materials can only inherit a perovskite crystal structure when the ion radius between the A and B cation are in a certain tolerance; the so called Goldschmidt tolerance factor.

$$t = \frac{r_a + r_X}{\sqrt{2}(r_b + r_X}$$

Equation 5: Goldschmidt tolerance factor

With r_a as the radius of the A cation, r_B of the B cation and r_X the radius of the anion. The tolerance factor must be in between 0.9 and 1 for a cubic structure and forming an undistorted lattice. In this ideal structure the B cation has a 6 – fold coordination surrounded by an octahedron of anion and the A cation has a 12-fold cuboctahedral coordination.

Following Figure 5 shows the crystal structure of an organic metal halide perovskite whereas “B” corresponds to a divalent lead cation, “A” to the monovalent methylammonium ($CH_3NH_3^+$) and “X” corresponds to iodide. The shown $MAPbI_3$ crystal structure was the first material implemented for a solar cell device[17].

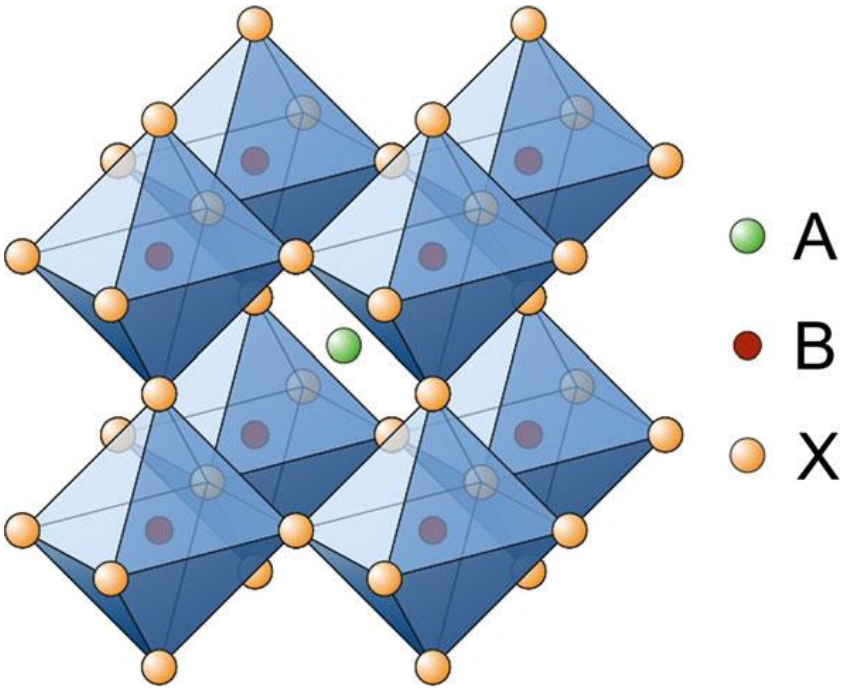

Figure 4: general perovskite structure with a halide as anion, © Sebastian Höfler[18]

The ability to be formed by several different elements opened up a new bunch of materials for solar cells. By substituting iodide with chloride and/or bromide to $MAPbCl_3$ and $MAPbBr_3$ respectively, the ion radius decreases and the band gap increases from 1.53 eV to 2.24 eV and 2.97 eV, respectively[19]. Replacing the A cation with formamidinium (FA, $CH_5N_2^+$) expansion of the lattice occurs and therefore, a lower bandgap is the result, inheriting a cubic perovskite structure[20,21].

A perovskite solar cell device consists of three parts; the perovskite which is the absorber material, an electron-transport layer (ETL) and a hole- transport layer (HTL).

The absorber layer, located between the HTL and ETL, is responsible for the generation and sufficient separation of the electron and hole. It must be a semiconductor material absorbing wavelengths of light in the range of the visible light and above (400 – 1000 nm) and must be able to perform the photovoltaic effect. The material should be free of Schottky and Frenkel defects making it a good conductor in the presence of a potential[22].

The ETL, needs to fulfill certain properties. Most importantly it needs to be able to extract electrons from the absorber material, while hinder holes to pass through to the electrode. In this so called p.i.n. structure (positively-doped, intrinsic, negatively-doped layer) the positively doped layer is mounted where the irradiation is passing through, before reaching the absorber material, and needs to be transparent therefore. In perovskite solar cells, a *n*-doped layer corresponds to an electron-transport layer without actually being negatively doped. Positive and negative doped description comes from silicon solar cells which are partly doped on the top and bottom of the absorber layer. For efficient extraction of the electrons the conduction band of the electron layer should be around or slightly lower than the conduction band energy level of the absorber material[23].

The hole-transport layer (HTL) is the counterpart to the ETL, extracting holes from the absorber layer towards it, resulting in a good charge separation together with the ETL. The HTL extracts the holes from the absorber material by having the energy level of the valence band of the HTL slightly higher than of the absorber. The hole-transport layer should also work as an electron blocking layer.

2.4. State of the art lead perovskite solar cells

In the past four years, the attention towards perovskite solar cells evolved rapidly due to fast increase of their power conversion efficiency (PCE) of up to 22 %[24] for organic-inorganic lead halide perovskite solar cells. Main reasons for their rapid growth includes defect tolerant properties of the material[25] which is leading to long carrier diffusion lengths[26], a low-cost alternative in fabrication due to solution processability, and an improved performance of solar cells by changing the device architecture[27,28,29] crystallization[30,31,32] and composition,[33,34,35] and tuning the bandgap.

Partial substitution of iodide with bromide increased the efficiency by tuning the band gap; though a major concern of bromide enriched perovskites is its low stability. Additionally, using a double cation by mixing FA into MA efficiencies for $FA_{0.66}MA_{0.33}Pb(Br_{0.33}I_{0.66})_3$ of up to 20.7% was achieved[36]. Using triple or quadruple A cations in tiny amounts, a further increase of PCE was achieved. “A” cations such as rubidium, which are found to be not photovoltaic active when implemented in a RbPbI-perovskite, are added to stabilize black phases of FA perovskites[37]. As theoretical studies have revealed, corner-sharing BX_6 octahedra in a three-dimensional network are a main factor for superior photovoltaic properties of lead based perovskites[38,39]

The instability under ambient humidity levels and the toxic heavy metal (Pb) are the major drawbacks for the ultimate commercialization of lead based perovskite technologies.[40,41,42] Replacing lead with another metal to form lead-free photovoltaic active perovskites absorber materials fell in the interest of many research groups. Substitution with a trivalent metal cation such as Bi or Sb leads to form a perovskite structure with the general formula $A_3C_2X_9$.

2.5. State of the art lead-free perovskite solar cells

2.5.1. Tin perovskite solar cells

Investigation for alternative metals to substitute lead directly lead to tin. The similar s^2 valence electron configuration to Pb^{2+} in combination with a similar ionic radius (Pb^{2+}: 119 pm, Sn^{2+}: 110 pm[43]) made Sn^{2+} ideal for replacing the toxic metal with an often presented nontoxic alternative. Bearing similar conditions as lead makes it possible for tin to form a perovskite with the basic formula $ASnX_3$. The dimensionality and connectivity of the formed perovskite lattice can be greatly affected by the functionality and the size of the A cation as well as the use of different halides[44]. While using a small monovalent A cation such as methylammonium and formamidinium the formation of a three-dimensional structure is preferred, larger ones like cyclobutylammonium causes a reduced dimensionality forming either two-dimensional layered, or one dimensional chain-like, or zero-dimensional structures[45].

So far a PCE of over 8 % for tin solar cells were reported[46] with a device architecture based on bathocuproine (BCP) as ETL and PEDOT:PSS as HTL and the absorber material consisting of $(FA)_{0.75}(MA)_{0.25}SnI_3$. A V_{OC} of 0.61 V was obtained by bearing a low band gap of only 1.26 eV. The J_{SC} was found to be around 21.2 mA/cm^2, while the fill factor was around 62.7 %. The bandgap can be moreover engineered by substituting more FA with MA obtaining various bandgaps in the range between 1.26 to 1.36 eV[46].

The main drawback is the chemically instability of tin halide perovskites causing Sn^{2+} to oxidize in ambient conditions to more stable Sn^{4+}. Consequently, oxidation of the divalent tin impedes the charge neutralization of the perovskite causing degradation and formation of oxides and hydroxides of tin, as well as Sn^{4+} leads to hole doping of the perovskite material[47,48]. To overcome this stability issue, encapsulation of the device is necessary as well as inert processing. Another possibility is using double perovskites A_2SnX_6 where Sn is present in its 4+ state[49].

2.5.2. Bismuth perovskite solar cells

Another candidate for replacing lead is bismuth, which is supported by various parameters such as an isoelectronic configuration ($6s^2$ $6p^0$) of the trivalent Bi^{3+} ion and the Pb^{2+} featuring the same $6s^2$ lone pair. In addition, bismuth shows a comparable ionic radius (Pb^{2+}: 119 pm, Bi^{3+} 103 pm[50]) and a similar electronegativity (Bi: 2.02, Pb: 2.33). However, due to its trivalent state bismuth cannot directly replace the divalent lead ion in the perovskite structure. Bismuth halide perovskites exhibit similar to tin perovskites a huge structural diversity in terms of dimensionality ranging from three-dimensional double perovskite networks over two and one-dimensional layers and chains to zero-dimensional dimer units[51]. The basic formula of zero-dimensional bismuth halide perovskites is $A_3Bi_2X_9$ and crystallizes in the $Cs_3Cr_2Cl_9$ structure. The closet packing of A and X atoms in that structure leads to stacked AX_3 layers occupying two thirds of an emerging octahedral site, while the last third are vacant. Subsequently, complex $Bi_2X_9^{3-}$ anion clusters are formed from pairs of obtained face sharing BiX_6 octahedra[52].

The most studied bismuth halide perovskite is the solution process able $(MA)_3Bi_2I_9$, which consists of pairs of face sharing BiI_6 octahedra, then forming isolated metal halide dimer units $Bi_2I_9^{3-}$ surrounded by disordered $CH_3NH_3^+$ ions[53]. Photovoltaic devices have been explored in planar and mesostructured configurations varying in the different use of HTL and ETL. Up to now, PCE of 1.64 % for $MA_3Bi_2I_9$ was achieved[54]. with a decent fill factor of up to 79 %, a V_{OC} of 0.83 V and J_{SC} of 3 mA/cm^2.

Drawback of this highly efficient Bi-based perovskite solar cell is the need of a high vacuum while depositing the BiI_3 films on the substrate instead of a solution based process. While solar cells with a spin coating process are cheaper and easier to handle, the efficiency suffers due to ineffective charge separation[55].

2.5.3. Antimony perovskite solar cells

The attention for antimony perovskite solar cell with the general structure $A_3Sb_2X_9$ rose with first accomplishments of Bi-based solar cells. The antimony cation has a similar electronic configuration alike the Pb cation but a trivalent state. Therefore, it might exhibit long carrier lifetimes[56] just as Bi, making it a promising photovoltaic material.

This statement was approved by investigating $Cs_3Sb_2I_9$ as photovoltaic active material. The 3+ state of antimony constraints the ability to form a 3D corner sharing perovskite. Instead, a dimer structure or a layered structure depending on the formation process is formed. The promising layered structure for photovoltaic activity although cannot be formed in a solution based process[57], since it forms the favorable dimer instead. In addition to the lack of solution processability, $Cs_3Sb_2I_9$ forms deep defects limiting the V_{oc} below 0.2 V and the current density below 0.2 mA/cm^2.

An obvious alternative to $CH_3NH_3PbI_3$, the antimony derivative was also investigated regarding its optoelectronic properties. Other than the $Cs_3Sb_2I_9$-perovskite the methylammonium based material is suitable for solution-process. But other than Pb-perovskites, hexagonal shaped crystals precipitate with a grain size of over 50 µm when no antisolvent is used[58] leaving parts of the layer uncovered. Using an antisolvent such as toluene, while spin coating, a pinhole free thin layer was obtained. A V_{oc} of 890 mV was reached with a decent fill factor of 55 % but however low photocurrent densities of only 1.1 mA/cm^2.

With the successful fabrication of solar cells using $(CH_3NH_3)_3Sb_2I_9$, other A cations were investigated for Sb-perovskites. Due to previous reports a link between the A cation size and the formed structure in the case of ABX_3 compounds are suggested [59,60]. A smaller cation like Rb could lead to different phases in $A_3Sb_2I_9$ structure as well. The formation energy of the dimer and layered structure of Rb differs by 0.25 eV in comparison to Cs with only 0.1 eV, resulting preferred in the layered structure. This is caused by the smaller ionic radius of Rb and therefore occupying less space in between corner sharing octahedra.

Other than the methyl-ammonium derivative, the device setup of $Rb_3Sb_2I_9$ is inverse using compact and mesoporous TiO_2 as an electron-transport layer and the expensive, widespread Spiro-MeOTAD is used as an HTL[8]. Furthermore, to smoothen the thin layer a process was developed to increase the current. An antimony iodide solution in toluene (10 mg/mL) was dropped while spin-coating at the absorber material before dropping the antisolvent to remove an excess of SbI_3[8]. XRD shows for untreated films a preferred orientation along the (002), (004) and (006) planes. These planes are parallel to the corner sharing octahedra layers, which hinder the charge transport across the films leading to a direction perpendicular to the layers as reported for similar materials[57] and therefore low current densities compared to theoretical possible ones.

I/V characteristics of $Rb_3Sb_2I_9$ provides an PCE of 0.66 % with a decent fill factor of 56 % and rather high currents of 2.1 mA/cm^2 compared to $(CH_3NH_3)_3Sb_2I_9$, but a lower V_{OC} of 0.55 V.

Combining the thermal stability[8] of Sb-perovskites with theoretical currents of around 10mA/cm^2, $Rb_3Sb_2I_9$ is a promising candidate for further investigation as a potential candidate for lead-free perovskite solar cells.

3. Experimental:

In this section, the setups for the undertaken experiments are described. As the goal was to investigate and characterize antimony based perovskite absorber materials as photovoltaic active semiconductor in solar cells, preliminary experiments were done before electronic characterization.

Chemicals:

MAI was purchased from Dyesol. SbI_3, RbI and was obtained from Alfa Aesar and RbBr received from ABCR. All these chemicals had a purity of 99.999 % and obtained in the form of a powder. PEDOT: PSS Clevios P VP.Al 4083 was obtained from Heraeus. $PC_{70}BM$ was purchased from Solenne in 99% purity. Spiro-MeOTAD and FK-209 was bought from Sigma Aldrich with a purity of 99% and LiTFSi from ACROS Organics with a purity of 99 % as well. For the TiO_2 layer Ti (IV) isopropoxide from Sigma Aldrich with a purity of 97 % was used.

Preparation of the precursor solutions:

For any of these experiments preparation of precursor solution was crucial to form a perovskite. Due to the instability of antimony iodide at ambient conditions, all following process steps and measurements were done under inert N_2-atmosphere in an MBraun glovebox until specified otherwise. A solution with a concentration varying from 0.1 mol/L to 0.4 mol/L was prepared by dissolving AX and SbX_3 in *N,N*-dimethylformamide (DMF) and heated up to 70 °C for 2 hours while stirring. Subsequently, the solution was cooled and filtered through a PTFE filter (size 0.45 µm) before further use. As an A cation methylammonium ($CH_3NH_3^+$) and rubidium (Rb^+) was used and for the X anion bromide and iodide, respectively. The perovskite is then formed from the stoichiometric dissolved salt when deposited for spin coating treatments as to see in following formula.

$$\mathbf{3}\,\boldsymbol{AX} + \mathbf{2}\,\boldsymbol{SbX_3} \rightarrow \boldsymbol{A_3Sb_2X_9}$$

Equation 6: Formation of the perovskite

Preparation of the glass substrates:

Substrates were prepared as followed: A glass substrate for preliminary tests and an Indium-tinoxide (ITO) coated glass substrate (Resistance: 15 Ω, purchased from Luminescence technology Corp.) were first cleaned with

acetone, put in isopropanol and treated in an ultra-sonic bath for 30 min. Subsequently, it was dried over an N_2-stream and plasma etched the (ITO covered) surface with ozone for 3 min. Afterwards, the substrates were introduced into the glovebox ready for further processing.

Preparation of the treatment solution:
An SbI_3 solution (50 µL) was prepared by dissolving 10 mg SbI_3 in 1 mL toluene and heating at 70 °C for 30 min under stirring.

Preparation of c-TiO_2 solution:
Ti(IV)-isopropoxide (210 µL) and Ethanolamine (165 µL) was distributed in Methoxyethanol (3 mL) and stirred for 10 min prior filtering with a PTFE filter (0.45 µm).

3.1. Characterization

Antimony perovskites were characterized by their UV/VIS spectra, their structure was determined by X-ray diffractometry as well as their surface roughness and optical appearance were investigated with a profilometer and an optical microscope. For these preliminary tests, it was not necessary to prepare the samples on ITO-coated substrates but simply on glass ones. Therefore, the substrates were cleaned and plasma etched as described in the beginning of Chapter 3.

3.1.1. UV/VIS absorption

For the UV/VIS spectra, a precursor solution of 0.1 mol/L was prepared and spin coated onto the substrate forming the absorber layer. As precursor solution $MA_3Sb_2I_9$, $Rb_3Sb_2I_9$, $Rb_3Sb_2I_{9-x}Br_x$ (x = 1, 2 and 3) were used and spin coated with following parameters.

Table 1: General spin coat parameters for UV/VIS absorption

Speed (rpm)	Acceleration (rpm/s)	Duration (s)	SbI_3-sol. (µL) after 3 sec	Antisolvent (µL) after 30 sec
4000	1500	60	50	70

The spin coated substrates were heated for 10 min at 120 °C and the UV/VIS spectra were measured outside the glovebox with a Perkin Elmer Lambda 35 UV/VIS spectrometer from a range of 340 to 800 nm using a scanning speed of 480 nm per minute. As background and baseline an uncoated glass substrate was used.

3.1.2. Profilometer

The thickness and roughness of the substrates were measured using a DektakXT Bruker profilometer with 12.5 µm radius stylus. The data acquisition was performed with a scanning speed of 100 µm/s for 10 s and a stylus force of 3 mg.

3.1.3. Optical Microscope

The surface of the samples was visually observed if they obtain any pinholes in the layer. The samples were prepared in the same way as the UV/VIS samples explained. For the observation a microscope BX60 from Olympus was used.

3.1.4. XRD-measurement

For XRD measurements, glass substrates were prepared according to Chapter 3. A precursor solution of different materials was spin coated and annealed as followed. 25 µL of the precursor solution (0.4 mol/L) was deposited on the substrate, spin coated and annealed at 120°C for 10 min

Table 2: Spin coat parameters for XRD

Speed (rpm)	Acceleration (rpm/s)	Duration (s)	SbI_3-sol. (µL) after 3 sec	Antisolvent (µL) after 30 sec
4000	1500	60	50	70

The fabricated samples were then measured outside the glovebox under ambient conditions. X-ray diffraction measurements were conducted on a PANalytical Empyrean diffractometer in Bragg-Brentano configuration operated at 40 kV and 40 mA using Cu Kα radiation (λ = 1.5418 Å).

For $Rb_3Sb_2I_{9-x}Br_x$ (x = 0, 1, 2 and 3), samples were prepared on compact and mesoporous TiO_2 layers as described in 3.2.2. and measured under inert atmosphere under a graphite dome, while $MA_3Sb_2I_9$, was measured under

ambient conditions on glass only. The graphite dome is part of the heating stage DHS900 from the company Anton Paar.

3.2. Preparation of solar cells

As described in the beginning of the experimental section, a ITO-covered substrate was cleaned and plasma etched as well as a precursor solution and the SbI_3- solution for treatment were prepared.

Due to an inverse device setup, the order of the electron-transport layer and the hole-transport layer deposition were not always the same. Using PEDOT:PSS as an HTL, the HTL is deposited first on the substrates. An annealing step at 150 °C makes this necessary. Using TiO_2 as an ETL an inverse setup was done because of the required annealing step of the TiO_2 at 500 °C. Both materials have a high transparency in the UV/VIS spectra in common, which keeps the absorption prior the photovoltaic active layer to a minimum.

3.2.1. Device setup of solar cells using PEDOT:PSS

A ITO-covered glass substrate was cleaned as described in the beginning of Chapter 3. The substrate then was spin coated outside the glovebox with PEDOT:PSS (AL 4083) with following parameters followed by an annealing step for 10 min at 150 °C.

Table 3: Spin-coat parameters for PEDOT:PSS

Speed (rpm)	Acceleration (rpm/s)	Duration (s)	PEDOT:PSS (µL)
3500	1500	30	30

Afterwards the sample was introduced into the glovebox and spin coated with a precursor solution with a given concentration of 0.1, 0.2 and 0.4 mol/L containing following precursor, respectively; $MA_3Sb_2I_9$, $Rb_3Sb_2I_9$ and $Rb_3Sb_2I_{9-x}Br_x$ (x = 1, 2 and 3). 25 µL of the precursor solution was used with following spin coat parameters for the absorber layer:

Table 4: Absorber spin coat parameter for thin layer solar cells

Speed (rpm)	Acceleration (rpm/s)	Duration (s)	SbI_3-sol. (µL) after 3 sec	Antisolvent (µL) after 30 sec
4000	1500	60	50	70

Subsequently, the substrates were annealed at 120 °C for 10 minutes.

A solution of $PC_{70}BM$ (40 mg/mL) in chlorobenzene as an electron-transport material (ETM) was prepared and spin coated onto the substrate at 1000 rpm for 60 seconds.

To obtain contact with the ITO electrode when measuring, a small area of around 1 × 2 mm was scratched away on the edges of the substrate respectively before evaporating the electrode (Ag, 100 nm) on top of the $PC_{70}BM$. Evaporation of silver on the masked substrates lead to 6 solar cells with an area of 0.09 cm^2 respectively and two contacts for the ITO beneath. Evaporation of silver was done under vacuum (< 3 × 10^{-5}bar) and ambient temperature. The I/V characteristics of the fabricated cells were then determined with simulated sunlight inside the glovebox. IV-measurements were recorded using a dedolight lamp at 100 mW/cm^2 and a Keithley 2400 source meter. The measurement was done in a voltage range from -0.05 to + 1 V, with a delay of 100 ms before each data point and a maximum compliance of 100 mA.

3.2.2. Device setup of solar cells using TiO_2

A ITO-covered glass substrate was cleaned as described in Chapter 3. The substrate then was spin coated outside the glovebox with the prepared c-TiO_2 solution with following parameters followed by an annealing step for 30 min at 500 °C in a tube furnace.

Table 5: Spin-coat parameters for compact TiO_2

Speed (rpm)	Acceleration (rpm/s)	Duration (s)	c-TiO_2 solution (µL)
10000	4000	20	20

Subsequently, the substrate was spin coated with a TiO_2-nanoparticle containing solution in terpineol forming the mesoporous TiO_2 layer with the same spin coat parameters as the compact layer. Two different layers are needed because using only the mesoporous layer direct contact of the absorber material and the electrode would be given. Using only a compact layer the preferred big area of the mesoporous layer would be missing. The sample then was pre-annealed at

200 °C for 5 min on a heating plate before inserting in the tube furnace at 500 °C for 30 min.

Afterwards, the sample was introduced into the glovebox and spin coated with a precursor solution with a given concentration of 0.1, 0.2 and 0.4 mol/L containing following precursor respectively; $MA_3Sb_2I_9$, $Rb_3Sb_2I_9$ and $Rb_3Sb_2I_{9-x}Br_x$ (x = 1, 2 and 3). 25 µL of the precursor solution was used with following spin coat parameters for the absorber layer formation:

Table 4: Absorber spin coat parameter for thin layer solar cells

Speed (rpm)	Acceleration (rpm/s)	Duration (s)	SbI_3-sol. (µL) after 3 sec	Antisolvent (µL) after 30 sec
4000	1500	60	50	70

Subsequently, the substrates were annealed at 120 °C for 10 minutes.

As an HTL a Spiro-MeOTAD solution was prepared. Spiro-MeOTAD (17.2 mg), bis(trifluoromethane)sulfonimide lithium salt, 2 mg), FK-209 (tris(2-(1*H*-pyrazol-1-yl)-4-*tert*-butylpyridine)cobalt(III)-tri[bis(trifluoromethane)-sulfonimide]), 0.6 mg) and TBP (4-*tert*-butylpyridine, 1.34 µL) was dissolved in chlorobenzene (200 µL) and stirred 30 min prior further use with following spin coat parameters.

Table 6: Spin coat parameters for Spiro-MeOTAD

Speed (rpm)	Acceleration (rpm/s)	Duration (s)	Spiro-MeOTAD (µL)
4000	1500	20	20

To obtain contact with the ITO electrode when measuring, a small area of around 1 × 2 mm was scratched away on the edges of the substrate respectively before evaporating the electrode (Ag, 100 nm or Au, 80nm) on top of the Spiro-MeOTAD. Evaporation of silver on the masked substrates lead to 6 solar cells with an area of 0.09 cm^2 respectively and two contacts for the ITO beneath. Evaporation of silver was done under vacuum (< 3×10^{-5}bar) and ambient temperature. The I/V characteristics of the fabricated cells were then determined with simulated sunlight inside the glovebox. IV- measurements were recorded using a dedolight lamp at 100 mW/cm^2 and a Keithley 2400 source meter. The measurement was done in a voltage range from -0.05 to + 1 V, with a delay of 100 ms before each data point and a maximum compliance of 100 mA.

3.3. EQE

The external quantum efficiency gives information about the ratio between the incident light of a given wavelength to the obtained converted current. For that solar cells in the inverse setup as well as in the regular setup were fabricated according to 3.2.1. and 3.2.2. These solar cells were then measured outside the glovebox under ambient conditions. The received currents dependent on the incident wavelength are further discussed in 4.3. The EQE spectra were measured using monochromatic light from a MuLTImode4 monochromator (AMKO) equipped with a Xenon lamp chopped at 30 Hz. The signals (wavelength increment: 10 nm) were measured by a lock-in amplifier from Stanford Research Systems (Model SR830). as a reference a spectrally calibrated 818-UV/DB photodiode (Newport Corporation) was used.

4. Results and discussion:

Antimony- perovskite materials as absorber materials are investigated and discussed in this Chapter 4. The materials $MA_3Sb_2I_9$ and $Rb_3Sb_2I_{9-x}Br_x$ were characterized in regard to their absorption spectra and their crystal structure and orientation in Chapter 4.1. This was done via UV/VIS measurements and XRD measurements, respectively. Later on, solar cells were fabricated in different device setup and their I/V characteristics were determined in Chapter 4.2. Using different ETL and HTL combinations, such as TiO_2 layers in combination with spiro-MeOTAD, resulted in different device efficiencies. Different process parameters were investigated and compared as well. The EQE for the best working device setup is also discussed in Chapter 4.3.

4.1. Characterization of the absorber material

4.1.1. Determination of the UV/VIS absorption

The UV/VIS spectrum provided information about the absorption of the investigated material regarding incident wavelengths. By varying the element composition of the absorber layer the structure changed and therefore its specific spectra.

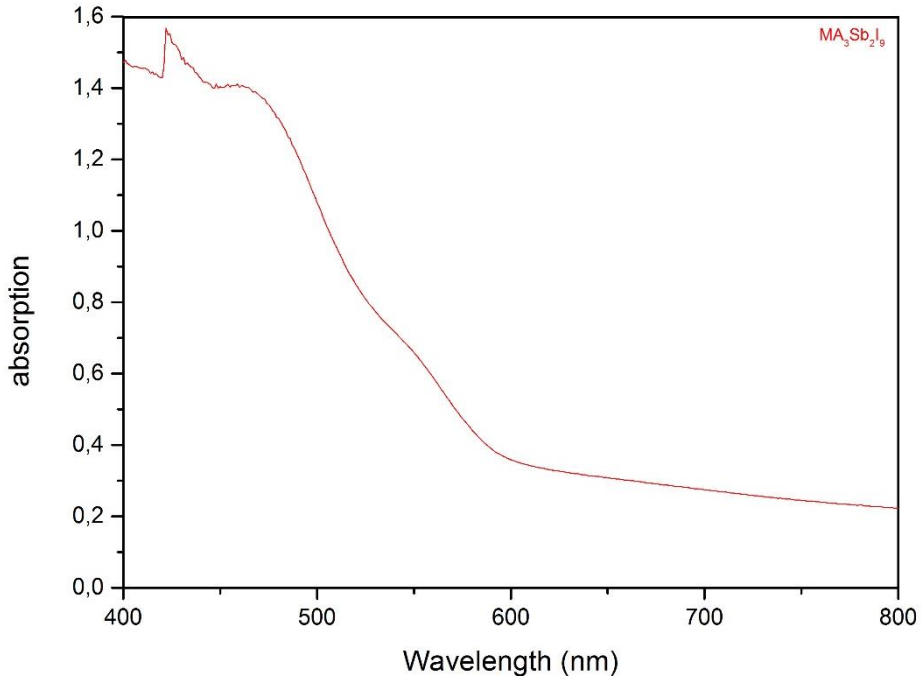

Figure 5: UV/VIS spectrum of $MA_3Sb_2I_9$

The UV/VIS spectrum of $MA_3Sb_2I_9$, shown in Figure 5, provides information about the photon absorption at different wavelengths. Determining the layer thickness using a profilometer, the maximum absorption coefficient of the material was calculated.

$$\alpha_\lambda = \frac{A_\lambda}{d} \times \ln(10)$$

Equation 7: Calculation of the absorption coefficient

A_λ = Absorption, d = layer thickness (cm), α_λ = absorption coefficient (cm^{-1})

For $MA_3Sb_2I_9$ $A_\lambda \approx 1.55$ at 422 nm, d ~ 340 nm resulting in an absorption coefficient $\alpha_{\lambda,max}$ of $\approx 1 \times 10^5$ cm^{-1}.

With the calculated absorption coefficient, a layer thickness with an optimum light absorption was estimated to be around 230 nm.

UV/VIS measurement and absorption coefficient calculation were also done for $Rb_3Sb_2I_{9-x}Br_x$ (x = 0, 1, 2, 3). Figure 6 shows the absorption coefficient as function of the wavelength.

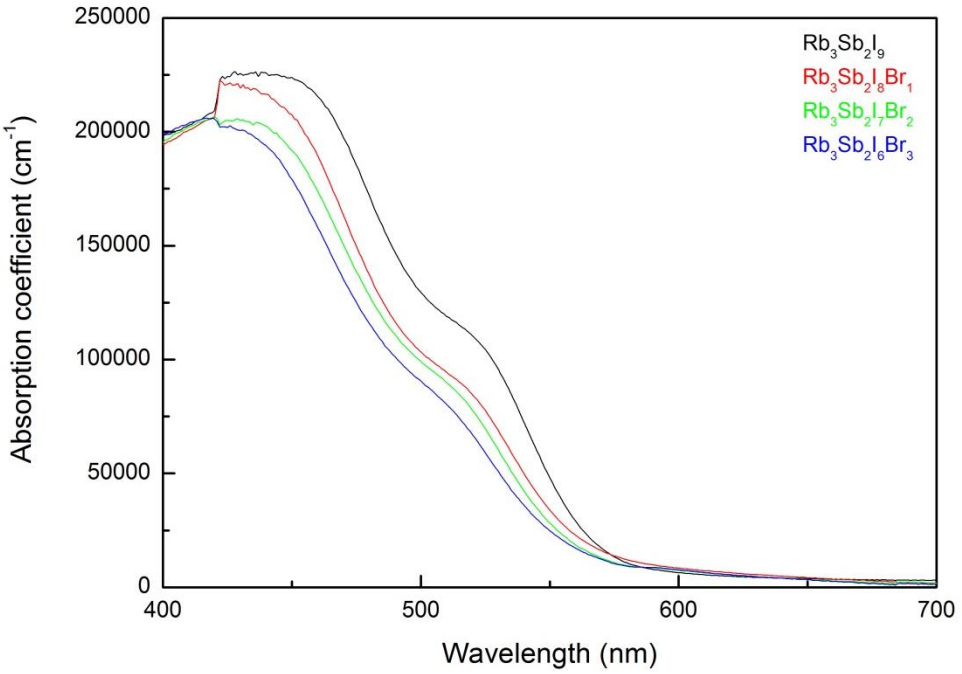

Figure 6: absorption coefficient of $Rb_3Sb_2I_{9-x}Br_x$ (x = 0, 1, 2, 3) against the wavelength

Table 7: Absorption coefficient of Rb-derivatives

Sample	$Rb_3Sb_2I_9$	$Rb_3Sb_2I_8Br$	$Rb_3Sb_2I_7Br_2$	$Rb_3Sb_2I_6Br_3$
Absorption coefficient$_{max}$ (cm-1) at λ = 422 nm	2.3×10^5	2.2×10^5	2×10^5	2×10^5

Figure 6 not only depicts the UV/VIS spectra of different absorber materials but furthermore, it shows the shift of the absorption towards lower wavelengths by increased bromide substitution. This absorption shift corresponds to the observable colour shift from red to yellow-orange at a constant layer thickness, as shown in Figure 7.

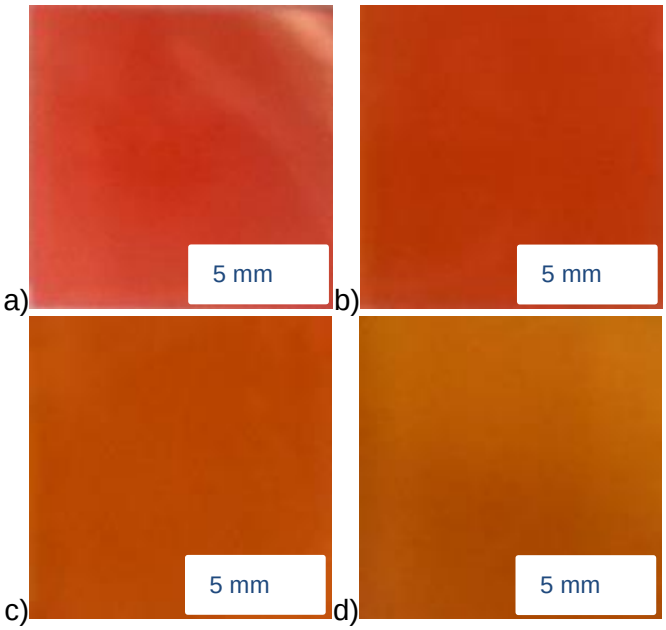

Figure 7: Picture of the Glass substrates of $RbSbI_{9-x}Br_x$ with a) X = 0 b) X = 1 c) X = 2 d) X = 3

The direct optical bandgap was calculated as well via the Tauc plot method. The intersection between the extrapolated linear straight with the x-axis was used in order to determine the direct optical bandgap. Plotting the photon energy against the absorption multiplicated with the photon energy at the power of two, a linear straight next to the onset provides the investigated information as shown in Figure 8 for $MA_3Sb_2I_9$ and for $Rb_3Sb_2I_{9-x}Br_x$ in Figure 9.

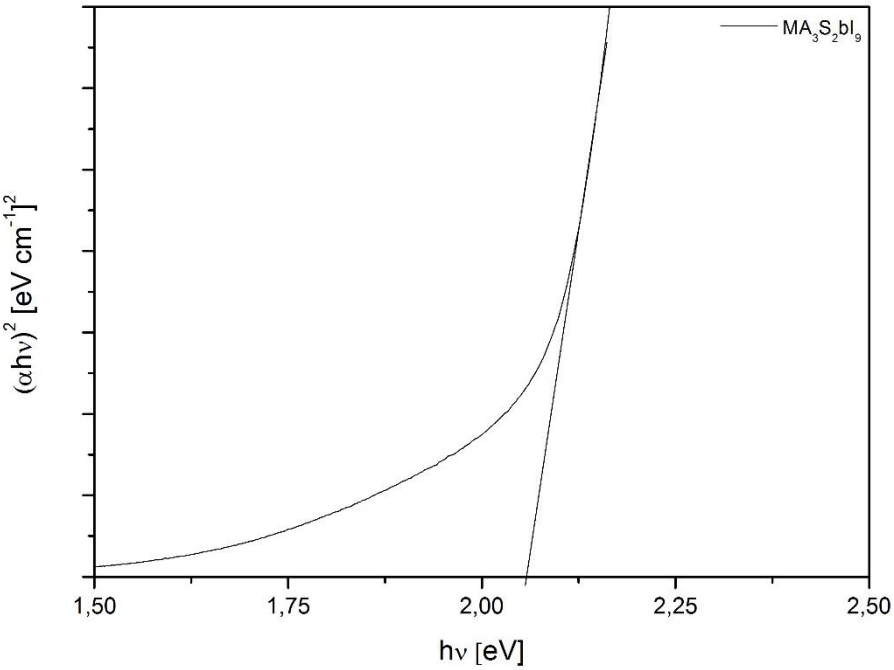

Figure 8: Tauc plot of the optical direct band gap of $MA_3Sb_2I_9$

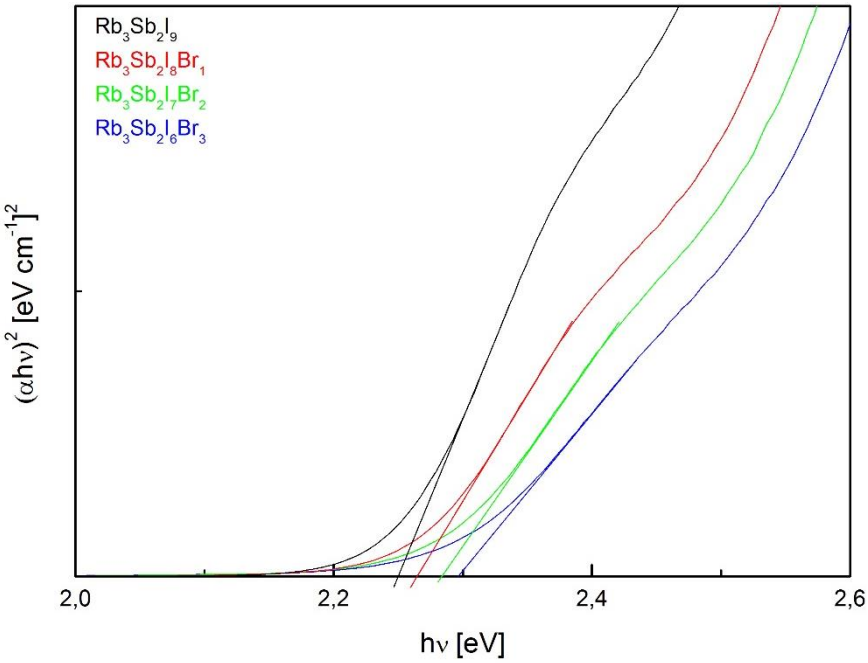

Figure 9: Tauc plot of the optical direct bandgap of $Rb_3Sb_2I_{9-x}Br_x$ (x = 0, 1, 2, 3)

Table 8: Optical direct bandgap of $MA_3Sb_2I_9$ and $Rb_3Sb_2I_{9-x}Br_x$ (x= 0, 1, 2, 3)

Sample	$MA_3Sb_2I_9$	$Rb_3Sb_2I_9$	$Rb_3Sb_2I_8Br$	$Rb_3Sb_2I_7Br_2$	$Rb_3Sb_2I_6Br_3$
Bandgap (eV)	2.06	2.24	2.27	2.29	2.30

As expected, the bandgap for higher bromide substituted materials like $Rb_3Sb_2I_6Br_3$ was higher than for the non-substituted $Rb_3Sb_2I_9$, as shown in Figure 9 and Table 8. This is consistent with the observation by the naked eye due to an absorption shift to lower wavelength and therefore a more yellowish substrate.

$MA_3Sb_2I_9$ with a direct optical bandgap of 2.06 eV is lower compared to $Rb_3Sb_2I_9$. Using rubidium instead of methyl ammonium, as the A cation, significantly increases the bandgap to 2.24 eV. An increase of the bandgap by using bromide partially in the Rb-perovskite can be noticed as well. This can be explained due to the smaller ionic radius of the bromide compared to the iodide. This increase of the bandgap could also increase the V_{OC}, when used as absorber material in solar cells.

4.1.2. XRD of the perovskites

To gain more information about the absorber material, XRD measurements were done to determine the crystal structure and the preferential orientation of different absorber materials. The use of an antisolvent (toluene) and a SbI_3-solution for smooth layer preparation while spin coating influences the formation of the crystal and its orientation. For the solution-treated substrate more peaks compared to the untreated reference can be distinguished. The orientation of the Sb-perovskite is preferred in a perpendicular arrangement because it is oriented on the surface of the substrate. A perpendicular arrangement hinders charge extraction across the material for $MA_3Sb_2I_9$. The treated substrate therefore has a less distinct orientation. XRD measurements of $MA_3Sb_2I_9$ and $Rb_3Sb_2I_{9-x}Br_x$ are shown in Figure 10 and Figure 11.

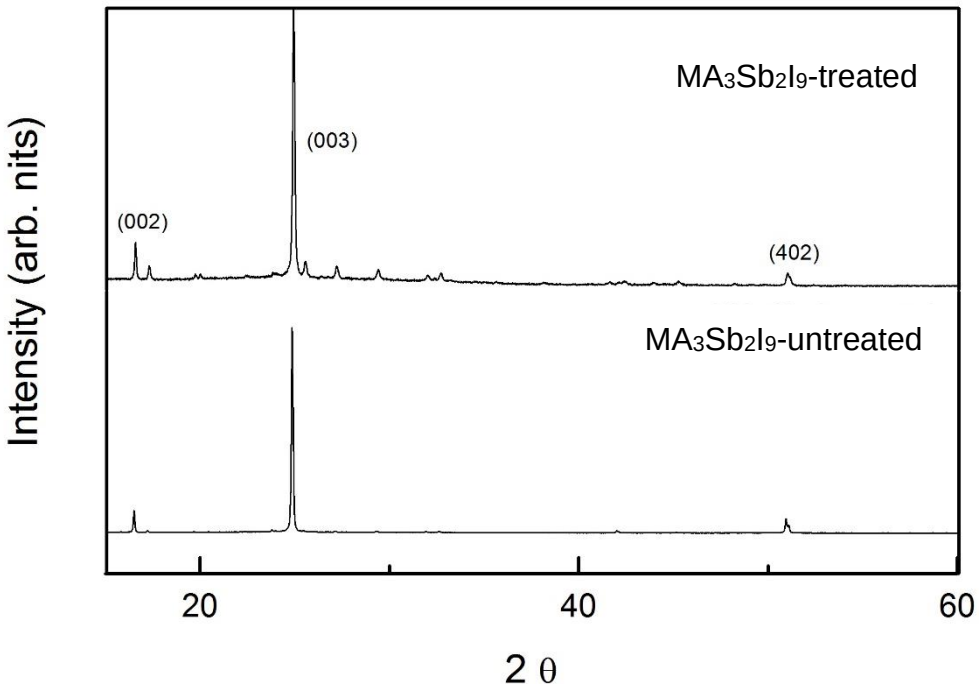

Figure 10: XRD figures top) $MA_3Sb_2I_9$ with an antisolvent and an SbI_3 treatment, bottom) $MA_3Sb_2I_9$ without antisolvent nor an SbI_3 solution

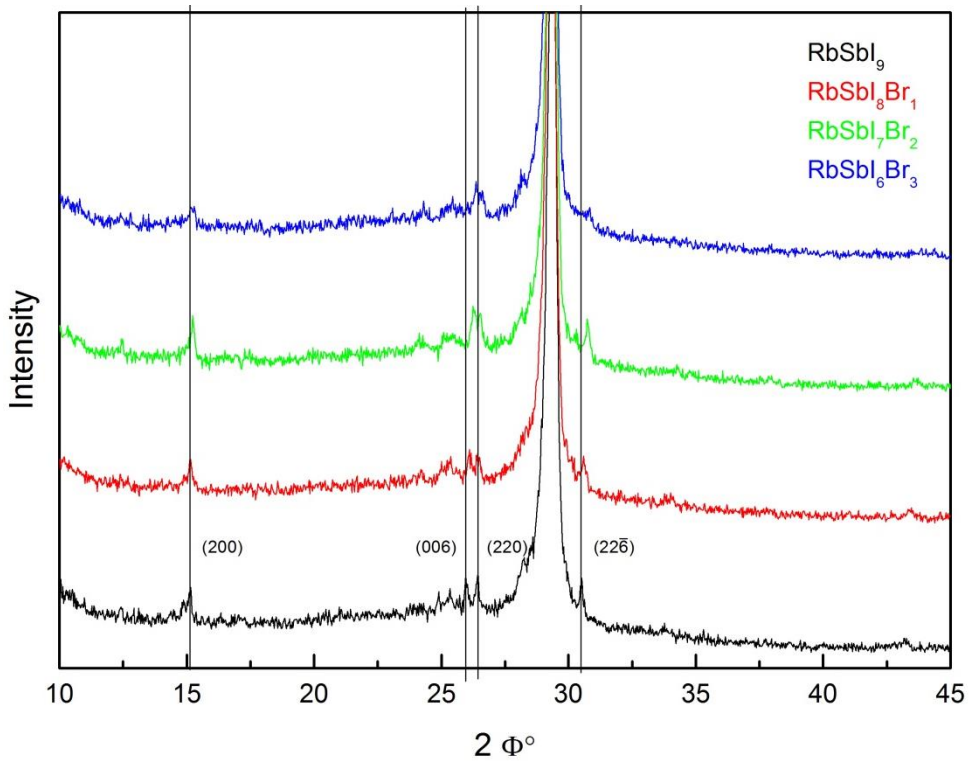

Figure 11: XRD of $Rb_3Sb_2I_{9-x}Br_x$ (x = 0, 1, 2, 3)

$MA_3Sb_2I_9$ shows a strong behavior of a preferential growth along the *c*-axis which hinders the charge transport across the absorber layer. Even the treated substrate exhibits a strong crystal growth orientation along the *c*-axis

For $Rb_3Sb_2I_{9-x}Br_x$ absorber materials, orientation not only along the *c*-axis but also along other axes across the absorber film are observed making it more promising for charge transport from one electrode to another.

Furthermore, Figure 11 shows a slight shift from lower angles as for the $Rb_3Sb_2I_9$ perovskite to higher angles by increasing bromide substitution. This shift to higher angles would indicate a decrease of the unit cells size. This trend matches the assumption, as the bromide ion has a smaller radius compared to the iodide radius which would lead to a denser packing in the unit cell. This also proves the insertion and replacement of bromide in the structure instead of forming another crystal structure.

4.1.3. Optical microscopy

A working solar cell is dependent on a pinhole-free surface. Due to pinholes in the layer a short circuit is likely, leading to a failure of the solar cell. The chances for pinhole-free substrates are much higher to work well as a solar cell. The surface of the absorber materials without the use of an antisolvent were examined, as shown in Figure 12.

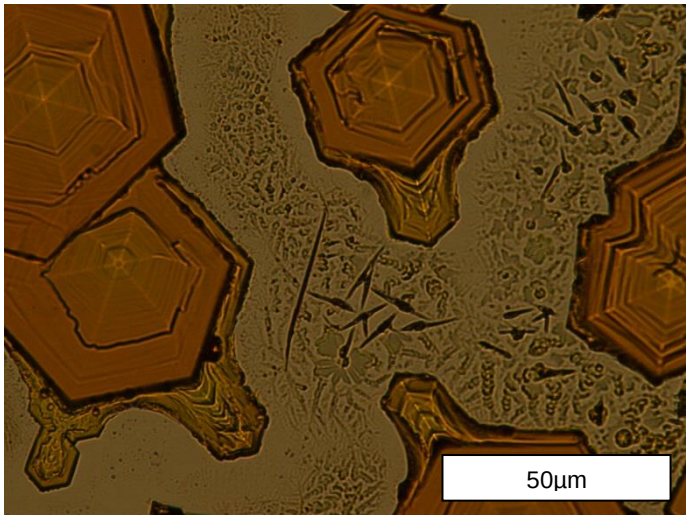

Figure 12: $MA_3Sb_2I_9$ surface without antisolvent

Crystals with a size of about 45 µm were observed. In general, the bigger the crystal size is the better the charge transportation would be, but hence of the fast crystallization and their size most of the surface is not covered with any absorber material at all, which makes it impossible to obtain a smooth homogeneous surface. By adding small amounts of an antisolvent (70 µL) to the absorber layer while spin coating, the crystallization and therefore the preferred crystal orientation is disturbed. This causes smoother pinhole-free surface as depicted in Figure 13.

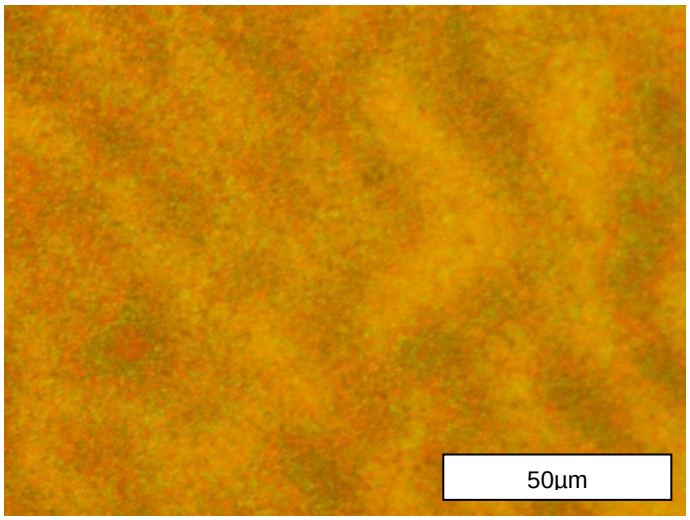

Figure 13: $MA_3Sb_2I_9$ with antisolvent

$Rb_3Sb_2I_{9-x}Br_x$ (x = 0 - 3) were investigated as well. As antisolvent toluene and a SbI_3 solution as treatment were used. Figure 14 shows the surface of $Rb_3Sb_2I_{9-x}Br_x$ (x = 0 and 3), respectively.

a) 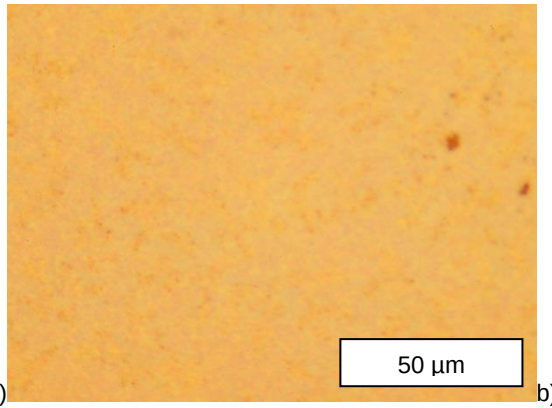

b) 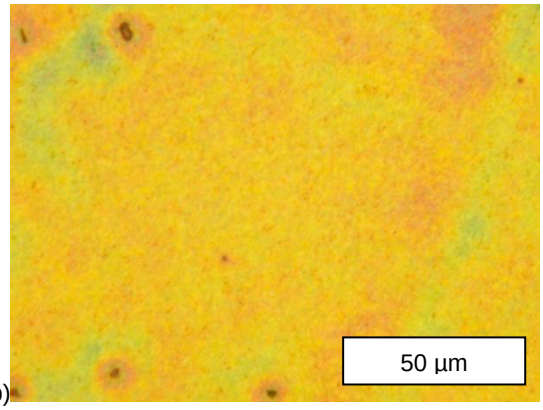

Figure 14: Surface of a) $Rb_3Sb_2I_9$ and b) $Rb_3Sb_2I_6Br_3$

As Figure 14 shows, these materials are a promising semiconductors for application in solar cells. Quite smooth surfaces without pinholes and no indication for a large crystal formation were prepared.

4.1.4. I/V characteristics of $MA_3Sb_2I_9$ and $Rb_3Sb_2I_9$

Solar cells were prepared and measured to prove if a photovoltaic activity is given and quantitatively presented if so. $MA_3Sb_2I_9$ solar cells were fabricated in an normal setup with TiO_2 as electron layer and Spiro-MeOTAD as HTL, and in an inverse setup on PEDOT:PSS as HTL and $PC_{70}BM$ as ETL. Silver and aluminum were deposited as electrode, respectively. Although $MA_3Sb_2I_9$ possesses all needed characteristics for a photovoltaic active absorber material, it was not

possible to obtain a current in any solar cell setup. In literature, a device setup was fabricated as followed[58]: glass/ITO/PEDOT:PSS/$MA_3Sb_2I_9$/$PC_{61}BM$/ZnO-NP/Al.

The tested device setup were glass/ITO/PEDOT:PSS/$MA_3Sb_2I_9$/$PC_{60}BM$/Al and glass/ITO/PEDOT:PSS/$MA_3Sb_2I_9$/$PC_{60}BM$/Ag and with $PC_{70}BM$, respectively. The solar cells fabrication between the literature and the fabricated solar cells differ only slightly from each other, but it influences the efficiency negatively leading to a failure of the device.

$Rb_3Sb_2I_9$ solar cells were prepared on PEDOT:PSS as discussed in the experimental part to gain first insight of the activity of the absorber material, as shown in Figure 15.

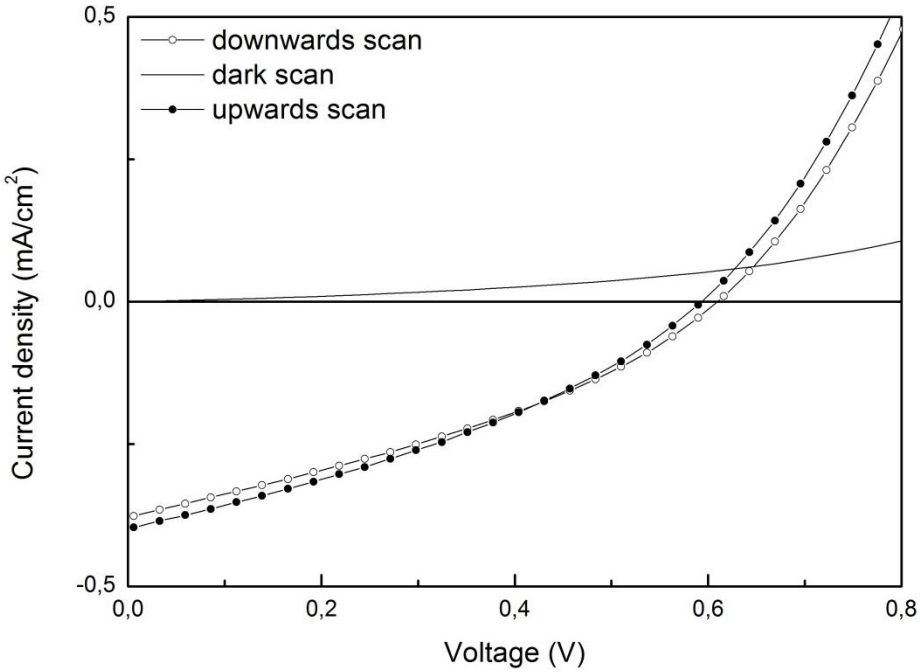

Figure 15: First working $Rb_3Sb_2I_9$ solar cell

Table 9: I/V characteristic values for first working $Rb_3Sb_2I_9$ solar cells

Sample	V_{OC} (V)	J_{SC} (mA/cm²)	FF	PCE (%)
Upwards scan	0.59	0.40	0.34	0.08
Downwards scan	0.61	0.37	0.33	0.08

A decent open circuit voltage was achieved, while the J_{SC} and the FF is rather poor resulting in a PCE with room for improvement. Hysteresis occurs when $Rb_3Sb_2I_9$ is used as an absorber material. The upwards scan differs slightly from the downwards scan. A slight decrease in the fill factor and in the current density is noticeable, as well as the V_{OC} differs slightly by increasing from 0.59 to 0.61 V.

4.1.5. Summary

As the preliminary tests show, antimony based perovskite solar cells are not that easy to fabricate. As for $MA_3Sb_2I_9$, although literature shows the processability and fabrication of working solar cells, after several attempts no photovoltaic activity could have been measured. Despite that, preliminary tests such as the UV/VIS spectra show a good light absorption in the range between 400 – 600 nm. Furthermore, the measured optical bandgap of around 2.07 eV indicate the material as a possible photovoltaic active semiconductor. The X-ray diffractogram of $MA_3Sb_2I_9$ shows a distinct peak at around 25° 2θ with a preferential growth in the *c*-axis. Due to all these conditions and the ability to form smooth surfaces, the fabrication of a solar cell device should be possible. However, fabricating solar cell devices did not result in a single working solar cell.

For $Rb_3Sb_2I_9$, however, gaining comparable results in preliminary tests, the fabrication of solar cells with the same conditions worked. As for solar cells with Rb^+ as A cation the UV/VIS spectra range from 400 - 550 nm with a high absorption coefficient and slowly decreases with increased wavelength until only very low absorption at 600 nm can be distinguished.

4.2. Electronic characteristics of $Rb_3Sb_2I_{9-x}Br_x$ solar cell devices

The fabrication of $Rb_3Sb_2I_{9-x}Br_x$ perovskite solar cells was optimized by changing different parameters while processing to obtain a solar cell with a high overall performance. Filtering the precursor-solution, variation of the annealing temperature, ramp of the annealing temperature, the variation of the precursor's concentration, the usage of a SbI_3 treatment solution and the use of different device setups were investigated, resulting finally in a well working solar cell device. Following chapters provide the data of these experiments which were done during this master thesis.

4.2.1. Comparison of filtered and unfiltered Precursor solutions

A precursor solution (0.2 mol/L) of $Rb_3Sb_2I_9$ was prepared. One half was filtered and the other half was not. Solar cells were fabricated with these two different solutions in exact the same way with $PC_{70}BM$ as ETL and PEDOT:PSS as HTL. The corresponding I/V characteristics are shown below.

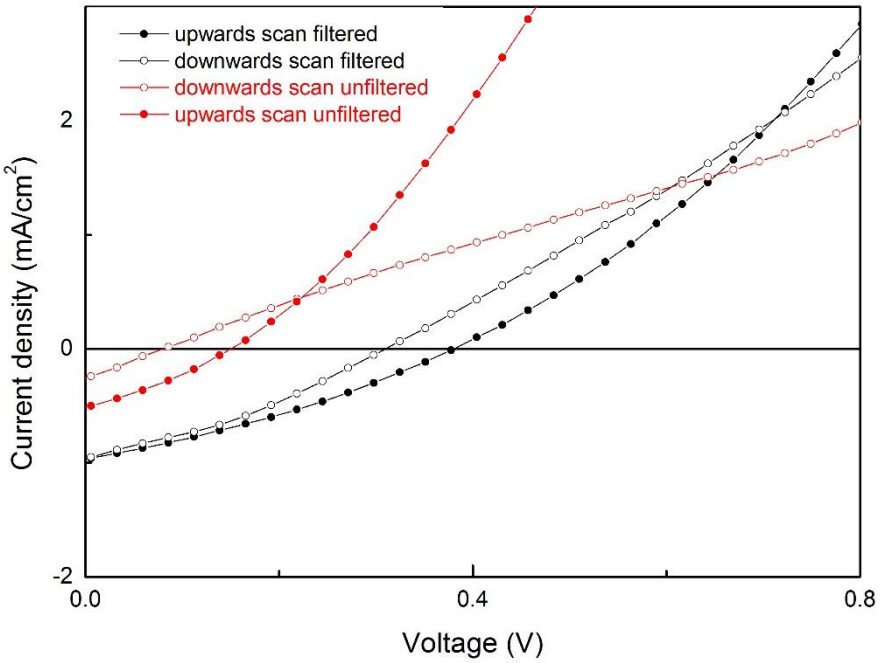

Figure 16: I/V characteristics of a solar cell with a filtered and an unfiltered $Rb_3Sb_2I_9$ precursor solution

Table 10: I/V characteristic values solar cells using a filtered and an unfiltered precursor solution

Sample	V_{OC} (V)	J_{SC} (mA/cm²)	FF	PCE (%)
Filtered	0.38	0.96	32	0.12
Unfiltered	0.14	0.50	35	0.02

Figure 16 and Table 10 show the comparison between these fabricated solar cells. A noticeable difference of the obtained results was observed. Impurities with no electronic conductivity such as dust particles might be distributed in the absorber material when unfiltered resulting in a bad device performance. The SbI_3 powder was sent to the laboratory in a glass ampule, which had to be opened by cracking the glass. Due to that fact, small glass particles might be distributed in the powder which are then filtered.

4.2.2. Influence of annealing temperature

To investigate the influence of the annealing temperature, $Rb_3Sb_2I_9$ solar cells were fabricated with the same setup and parameters except a variation of the temperature after spin coating the absorber layer onto the substrate. The absorber layers were annealed at temperatures of 70 °C, 90 °C and 120 °C as well as a non-annealed solar cell was prepared. By annealing the samples, the residual solvent diffuses through the absorber layer forming the perovskite structure concomitant with a change of colour. The concentration of the precursor solution was 0.2 mol/L. $PC_{70}BM$ and PEDOT:PSS were used as ETL and HTL, respectively.

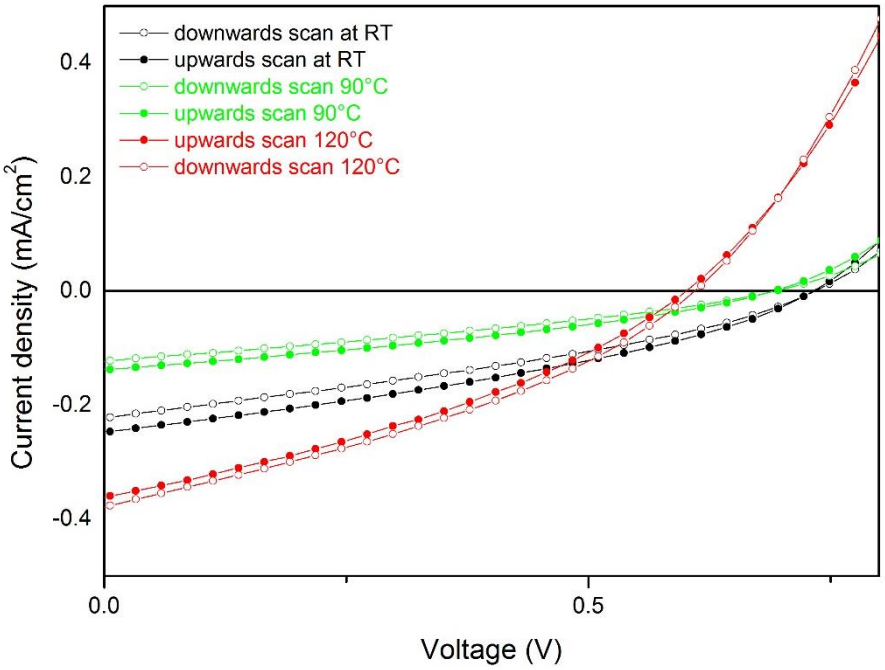

Figure 17 I/V characteristics of solar cells using different annealing temperatures

Table 11: I/V values of solar cells using different annealing Temperatures

Sample	V_{OC} (V)	J_{SC} (mA/cm^2)	FF (%)	PCE (%)
$RT_{up\ scan}$	0.72	0.25	35	0.06
$90°C_{up\ scan}$	0.69	0.14	33	0.03
$120°C_{up\ scan}$	0.59	0.36	35	0.07

Figure 17 shows a high voltage for the non-annealed and the 90 °C annealed sample with rather low currents, while annealing at 70 °C (I/V characteristics not shown in Figure 17)the substrate did not show a photovoltaic behavior. Annealing at 120 °C exhibits a high open circuit voltage as well as the highest current making this process-parameter the best working.

The non-annealed solar cell features an overall good performance. The appearance of the substrate is yellowish. The yellowish colour can be explained of the presence of residual solvent. The surface seems compared to the 120 °C substrate to be quite rough which might be an indicator for the formation of bigger crystals. Bigger crystals could decrease the amount of defect sites and grain boundaries, which would explain the high voltage.

Annealing at 90 °C might be insufficient to free the substrate from the solvent before spin coating the HTL. Consequently, under the following high vacuum treatment for evaporating the electrodes on the HTL, the residual solvent might cause an imperfect crystal lattice with Iodide vacancies and therefore deep traps. Even though an elevated temperature was used for annealing, solvent evaporation is still insufficient. The colour changed from yellow to an orange- red appearance.

At 120 °C the current density is nearly twice the amount compared to the second best, the untreated, solar cell but with lower V_{OC}. Overall it shows a better PCE and a smoother surface and is therefore more promising applying in a solar cell device. The colour changed during annealing from yellow to red. Moreover, the processability with this temperature annealing process is superior than any other due to the formation of smooth surfaces and therefore a better interlayer compatibility.

4.2.3. Treatment with an SbI_3-toluene solution while spin coating

During the spin coating step, the preformation of the layer is done. The performance of Sb-based solar cells can be influenced drastically by using an SbI_3 solution in toluene while spin coating.[8] This effect was tested experimentally providing the results in Figure 18.

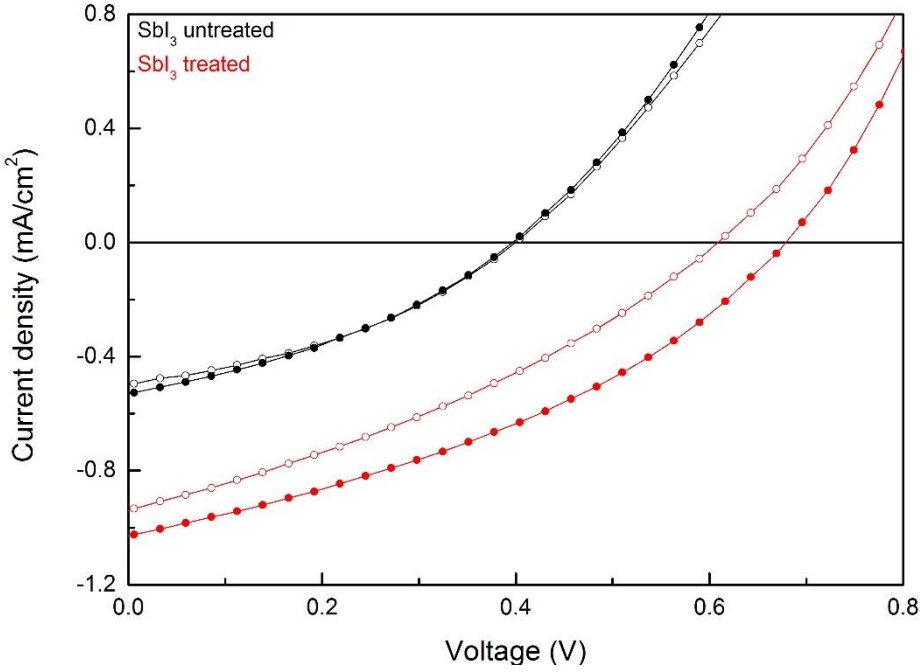

Figure 18 I/V characteristics of a SbI_3-solution treated and an untreated solar cell where ○ represents the downwards scan and ● the upward scan, respectively

Table 12: I/V values for a SbI_3-solution treated and an untreated solar cell

Sample	V_{OC} (V)	J_{SC} (mA/cm^2)	FF	PCE (%)
treated	0.66	1.02	37	0.25
untreated	0.40	0.53	34	0.07

Figure 18 shows the influence of the SbI_3-soution compared to the untreated one. One can distinguish the increased short circuit current of around 1 mA/cm^2, which is around twice the value of the compared solar cell. The V_{OC} increased drastically by around 65% as well. This SbI_3 solution treatment while spin coating decreases the vacancies of iodide in the crystal structure and provides not only higher currents but also influences the open circuit voltage positively.

After successfully implementing this process step, the amount of the ideal volume was investigated. A variation of volume of the treatment solution was used and compared to each other showing in following Figure 19. The concentration of the precursor solution was 0.2 mol/L. PEDOT:PSS and $PC_{70}BM$ were used as HTL and ETL, respectively.

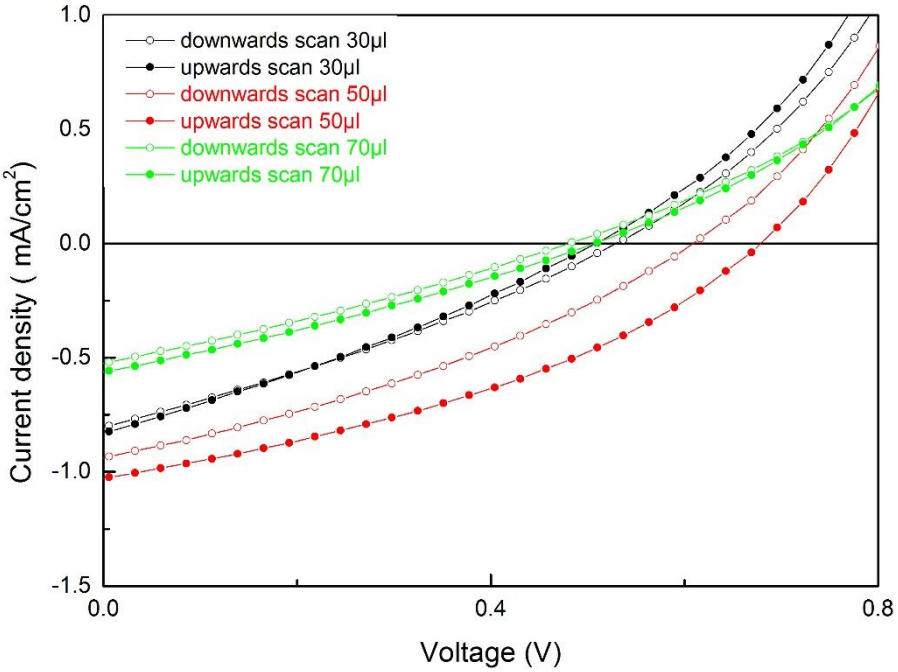

Figure 19 I/V characteristics of solar cells using a different amount of SbI_3 solution

Table 13: I/V values of solar cells using a different amount of SbI_3 solution

Sample	V_{OC} (V)	J_{SC} (mA/cm²)	FF	PCE (%)
30 µl	0.51	0.82	29	0.12
50 µl	0.67	1.02	37	0.25
70 µl	0.51	0.56	29	0.08

Figure 19 shows best working solar cells using 50 µL of the SbI_3 solution. Using more solution causes the J_{SC} to shrink to 0.5 mA/cm² and the V_{OC} to 0.5 V. similar with using a lower solution volume, the J_{SC} and the V_{OC} is decreased resulting in a decrease of PCE. A closer look to the 50 µL sample shows also a slightly better fill factor compared to others. This might be because of a better overall performance of the device.

4.2.4. Dependence of precursor concentration

The concentration of the precursor solution is a significant parameter for varying the thickness of the absorber layer. A higher precursor concentration result in a thicker layer, while a lower concentration reduce it. By knowing the optimal thickness, the concentration of the precursor can be varyied to obtain best conditions. It is also possible to vary the spin coating parameters, where a reduced spin coating speed gives a thicker layer. By changing this spin coating parameter, it happens to receive inhomogeneous and rough surfaces. Figure 20 shows the I/V characteristics for a solar cell with a precursor concentration of 0.2 mol/L and 0.4 mol/L, respecively.

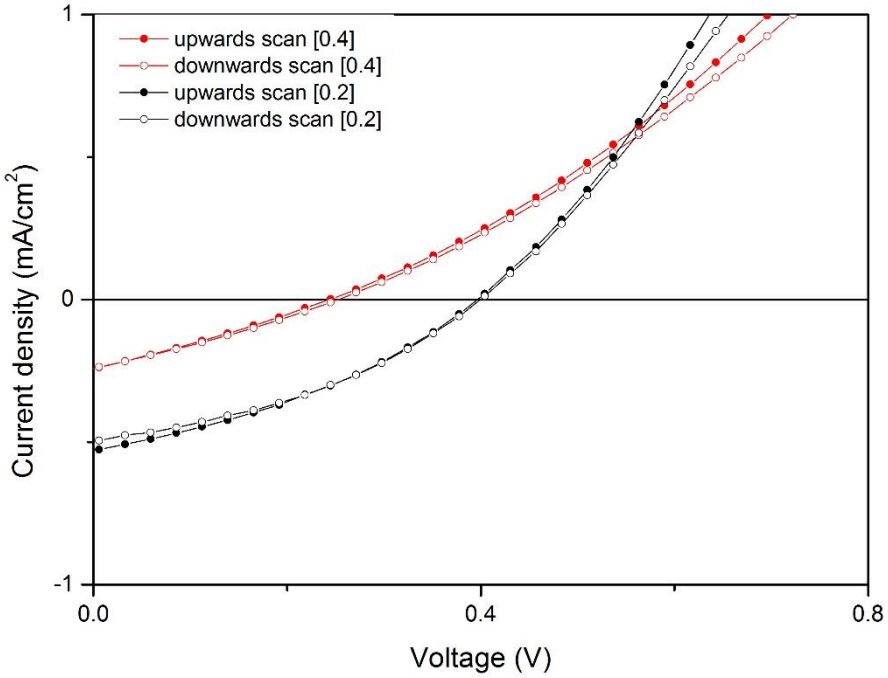

Figure 20: I/V characteristics of solar cells using different precursor concentration

Table 14: I/V characteristics of solar cells using different precursor concentrations

Sample	V_{OC} (V)	J_{SC} (mA/cm^2)	FF	PCE (%)
[0.2]	0.40	0.53	35	0.07
[0.4]	0.24	0.24	28	0.02

As Figure 20 depicts, the solar cell with [0.2] result in a higher J_{SC} than the higher concentrated one. This can be explained by comparing the thickness of the samples and the absorption coefficient. The layer thickness from the 0.2 mol/L to the 0.4 mol/L one is doubled having a thickness of 200 nm and 400 nm, respectively.

Using the [0.2] precursor solution the layer thickness is fitting the absorption maximum in the range between 400 – 500 nm very well, making it a perfect match for a good photovoltaic activity performance and a good charge extraction. With thinner layers, the path an electron must diffuse is kept to a minimum and the likelihood of non-radiative recombination is therefore reduced as well.

The V_{OC} might decrease for thicker solar cells due to longer pathways and an increased chance for electrons to get caught in a deep trap, which is a result of more iodide vacancies. Also, recombination is more likely, which reduces the performance of the fabricated solar cells using the precursor concentration of 0.4 mol/L.

4.2.5. Annealing with a temperature program

As already discussed, the annealing temperature is crucial for good working solar cells. Here, the influence using a temperature program will be discussed. The idea was to slowly heat the sample after spin coating the absorber layer to give the material time to rearrange in a better way gaining higher currents and a higher open circuit voltage. In Figure 21, a solar cell was heated at 20 °C per minute and compared with a solar cell annealed at 120 °C. The maximal temperature for all samples was 120 °C hold for 10 minutes.

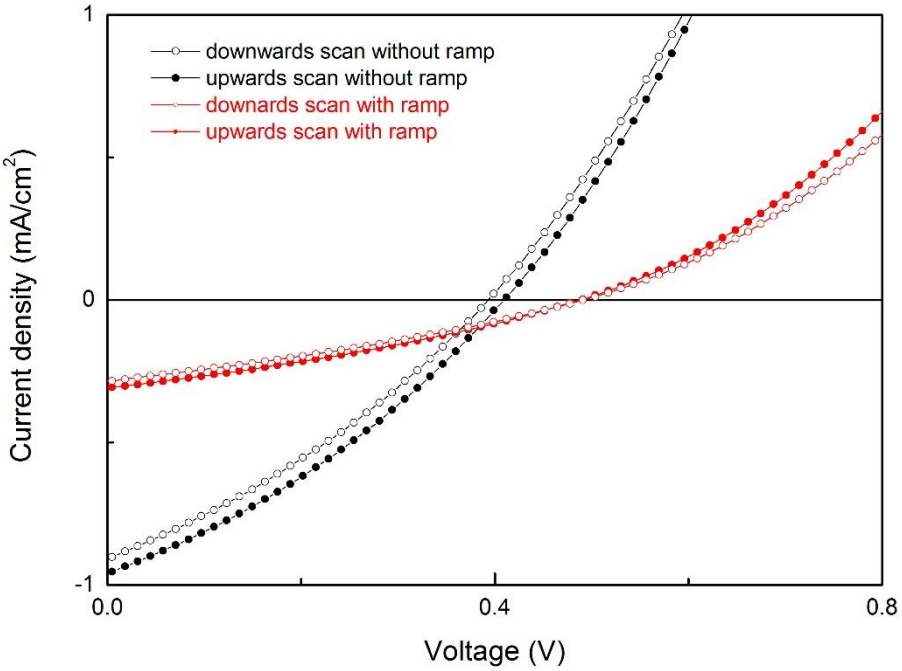

Figure 21: I/V characteristics of ramped and non-ramped solar cells

Table 15: I/V values of a ramped and a non-ramped solar cells

Sample	V_{OC} (V)	J_{SC} (mA/cm^2)	FF	PCE (%)
Ramped	0.49	0.31	32	0.05
Non-ramped	0.41	0.95	32	0.13

The performance of the temperature driven annealed solar cell is rather poor compared to the normal annealed one. The V_{OC} decreases from 0.49 V to 0.41 V, which is a decrease of around 20%. The J_{SC} is reduced to ~ 0.3 mA/cm^2, which is around a third of the original one.

4.2.6. Investigation of TiO_2 as electron-transport layer

Up to now, only a process variation for the absorber layer $Rb_3Sb_2I_9$ was examined. Another point of interest is the interface between the absorber layer and the ETL and HTL in the device setup, respectively and therefore solar cells with an alternative device setup were fabricated. The use of TiO_2 layer as an electron-transport material improves the performance of the device. Due to the mesoporous layer of TiO_2 the intercalation of the perovskite in between the pores comes along with a better electron extraction, due to short diffusion paths, and more efficient due to less non-radiative recombination. As a hole-transport layer Spiro-MeOTAD in chlorobenzene was used. The concentration of the precursor solution was 0.2 mol/L. As an ETL $PC_{70}BM$ (70 mg/mL) in chlorobenzene and as HTL PEDOT:PSS (40 nm) was used for the organic setup. For the inverse setup c-TiO_2 (80 nm) and m- TiO_2 (150 nm) as electron-transport materials and Spiro-MeOTAD as an HTL (70 mg/mL) in chlorobenzene were used. Figure 22 depicts the comparison of two $Rb_3Sb_2I_9$ absorber layers in different device setups.

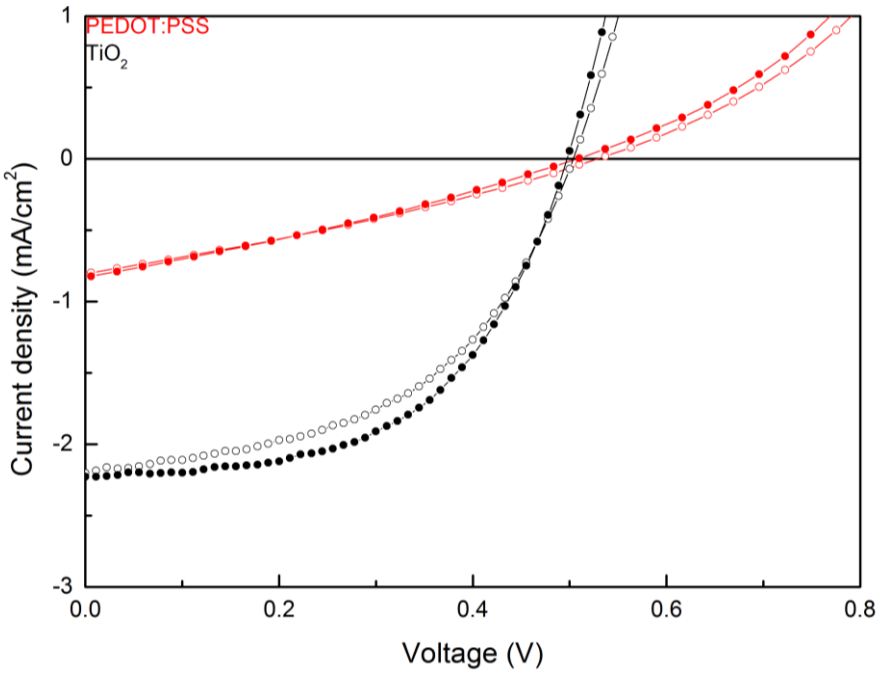

Figure 22: Comparison of the I/V curve between a device with following setup: ITO/ c-TiO_2/m-TiO_2/$Rb_3Sb_2I_9$/Spiro-MeOTAD/Ag and a device setup with ITO/PEDOT:PSS/ $Rb_3Sb_2I_9$/$PC_{70}BM$/ Ag

Table 16: I/V values of solar cells using a TiO_2 and a PEDOT:PSS setup

Sample	V_{OC} (V)	J_{SC} (mA/cm^2)	FF	PCE (%)
PEDOT:PSS	0.51	0.82	29	0.12
TiO_2	0.50	2.23	54	0.60

The performance of the TiO_2 based device setup compared to the PEDOT:PSS setup is superior. Reasons therefore are a bigger surface area between the absorber material and the ETL and a shorter diffusion length of the electrons through the absorber material. The main disadvantage thereby is the high annealing temperature of 500 °C. This annealing step is needed to remove the residual binder and in order to work properly.

4.2.7. Influence of multiple scan

The implementation of mesoporous TiO_2 as ETM has a direct effect on the absorber material. By applying an electromagnetic field, the absorber material seems to arrange in the mesoporous ETM. Repeating measurements show an improved diodic behavior and therefore increased FF as well as a better charge extraction, as depicted in Figure 23.

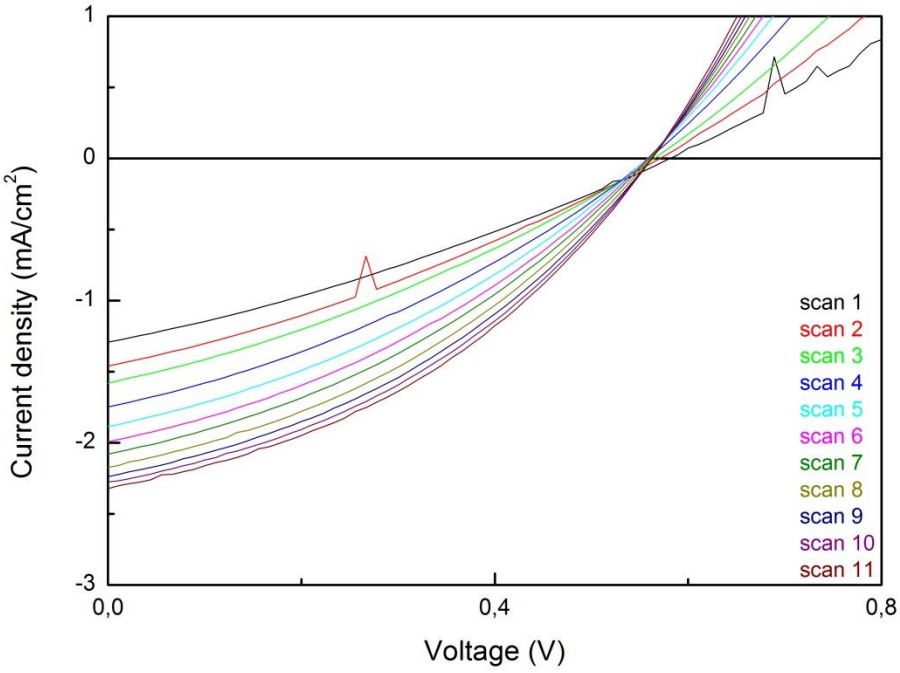

Figure 23: I/V characteristics of a solar cell by repeated scans

Table 17: I/V values of a solar cell by repeated scans

Sample	V_{OC} (V)	J_{SC} (mA/cm²)	FF (%)	PCE (%)
Scan 1	0.58	1.29	30	0.22
Scan 11	0.56	2.32	55	0.50

Due to repeated scans, the fill factor increased from 30% to a maximum of 55 %. The current density increased from 1.3 mA/cm² to 2.3 mA/cm², while the V_{OC} slightly decreased to 0.56 V.

Incident light also increases the temperature of the solar cell and therefore, also an increased activity of the material could occur. To exclude the influence of a temperature increase in the solar cell, a sample was stressed after the first measurement in an electric field at 3 V for 200 ms and scanned again obtaining the same result as the shown multiple scans.

4.2.8. Partially substitution of iodide with bromide

Substitution of the anion in the perovskite shifts the absorption spectra to lower wavelength as already discussed previously in 4.1.1. This is also observable in a macroscopic point of view by changing the colour of the perovskite from a deep red to an orange and ultimately to a yellow-orange appearance. The effect in a photovoltaic point of view should result in a decrease of J_{SC} and an increase of V_{OC}. The decrease of current is a result of the absorption-shift of the material because then less photons fulfill the requirements to perform the photovoltaic effect. A wider bandgap, which comes along with an absorption shift, should result in an increase of the V_{OC}. A series of partially substituted bromide solar cells with formula $Rb_3Sb_2I_{9-x}Br_x$ (x = 0, 1, 2, 3) was prepared and compared in following Figure 24 and Table 18.

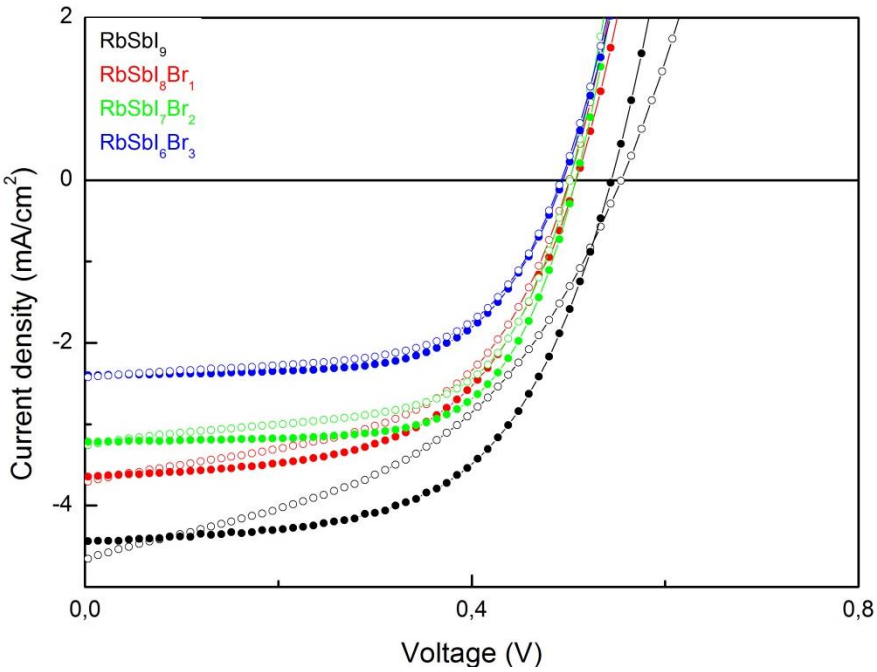

Figure 24: I/V Characteristics of solar cells using $Rb_3Sb_2I_{9-x}Br_x$ (x = 0, 1, 2, 3)

Table 18: Results of $Rb_3Sb_2I_{9-x}Br_x$ (x =0, 1, 2, 3) solar cells

Sample	V_{OC} (V)	J_{SC} (mA/cm^2)	FF (%)	PCE (%)
$Rb_3Sb_2I_9$	0.54	4.4	58	1.40
$Rb_3Sb_2I_8Br$	0.51	3.6	56	1.03
$Rb_3Sb_2I_7Br_2$	0.51	3.2	66	1.08
$Rb_3Sb_2I_6Br_3$	0.49	2.4	64	0.74

As Figure 24 shows, the J_{SC} is directly linked to the substitution of iodide with bromide. The V_{OC} did not behave as expected which lead to the assumption another effect must have taken place by increased bromide concentration.

The best performance shows the pure $Rb_3Sb_2I_9$ compound providing not only excellent currents but also the highest voltage. This is unexpected because of the substitution a higher voltage with increasing substitution was expected.

As expected, a decreased performance of $Rb_3Sb_2I_8Br$ compared to $Rb_3Sb_2I_9$ in terms of lower current densities were observed. However, the decrease of V_{OC} to around 0.51 V was a surprise. Hence to a lower voltage, the overall PCE could be increased. The fill factor of around 56% is slightly lower compared to the others.

By increasing the bromide concentration as for $Rb_3Sb_2I_7Br_2$ and $Rb_3Sb_2I_6Br_3$, the V_{OC} is comparable to the $Rb_3Sb_2I_8Br$ absorber material. The trend of decreasing current while having a nearly constant fill factor through all the samples lead to a lower PCE indirect proportional to the used bromide concentration.

To resolve the question of the unexpected V_{OC} decrease by adding bromide is argued by having a closer look on the UV/VIS spectra again.

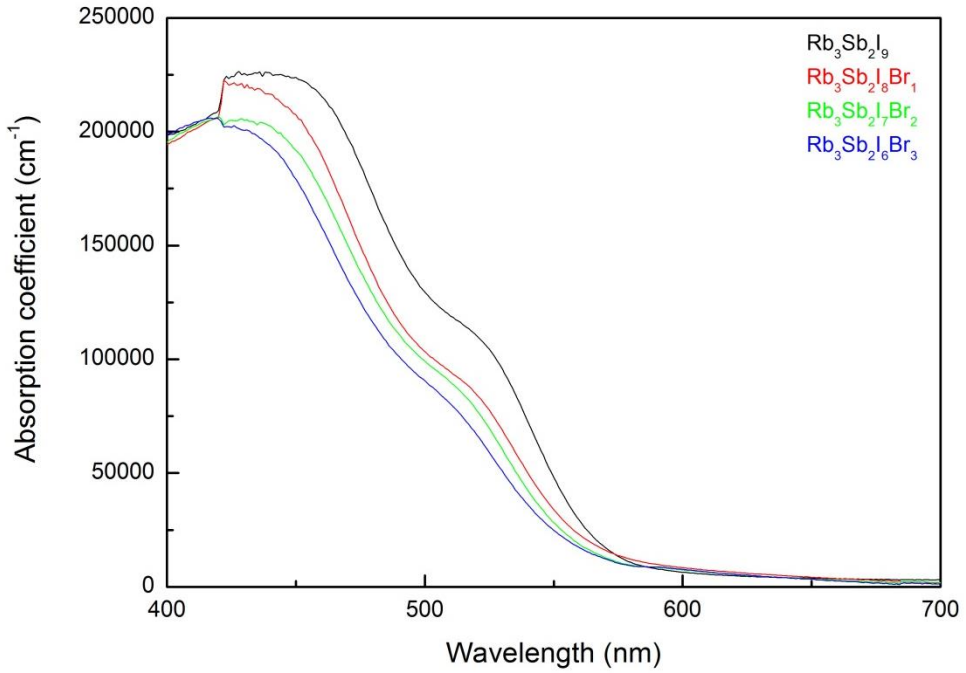

Figure 6: UV/VIS spectra of $Rb_3Sb_2I_{9-x}Br_x$ (x = 0, 1, 2, 3) materials

It happens to be not only a shift to lower wavelength but also the absorption spectra changes by increasing bromide substitution. In the unsubstituted Absorber at 520 nm a shoulder with an increased absorption is visible. This shoulder happens to get smaller by higher substitution. Due to that fact, the linear

slope seems to be more flat next to the onset which indicates a higher Urbach energy (E_U). By plotting ln (α) (α= absorption coefficient cm^{-1}) against hv (eV) the linear slope applied next to the bandgap provides information about the Urbach energy. The Urbach energy represents structural disorders, impurities and deep trap effects as well as excitons. The calculation and corresponding Figure 25 is shown below.

$$\ln(\alpha) = \frac{h\nu}{E_U} + \ln(\alpha_0)$$

Equation 8: Calculation of the Urbach energy

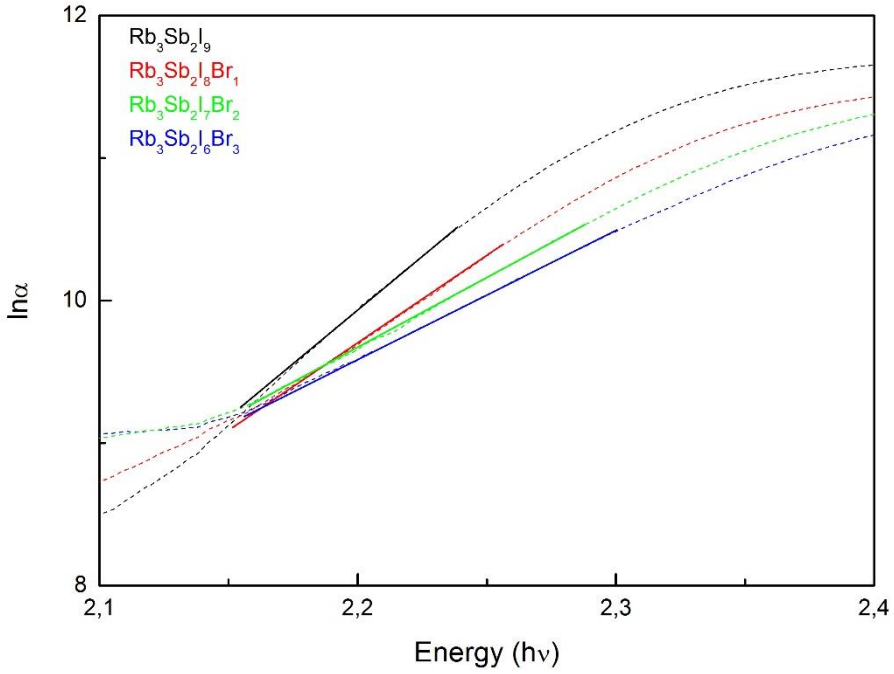

Figure 25: Urbach tail plot for $Rb_3Sb_2I_{9-x}Br_x$ (x = 0, 1, 2, 3) materials

Table 19: Urbach energy of $Rb_3Sb_2I_{9-x}Br_x$ (x = 0, 1, 2, 3) materials

	$Rb_3Sb_2I_9$	$Rb_3Sb_2I_8Br$	$Rb_3Sb_2I_7Br_2$	$Rb_3Sb_2I_6Br_3$
Urbach tail Energy (meV)	79	86	108	116

Previous Figure 25 shows an increase of the Urbach energy by increased bromide substitution. This leads to an increase of disorders in the material and therefore a decrease of the V_{OC} can be explained.

Due to the good obtained results the I/V characteristics for the best working solar cells were also measured while masked. Due to the fact, that the simulated sunlight source is around 50 cm away from the substrate, light beams can not be assumed to be parallel to each other, which influences te J_{SC} of the solar cell. Also an higher area of the absorber material compared to the real area of the cell is irradiated. This results in an higher absorption and therefore higher current densities. To circumvent this effect a mask slightly smaller than the cell area (mask: 2.9*2.9 mm^2, cell 3*3 mm^2) was put on top of the cell area and measured. To calculate the J_{SC} the new area has to be taken into account. Figure 26 shows the I/V characteristics of a solar cell with and without a mask.

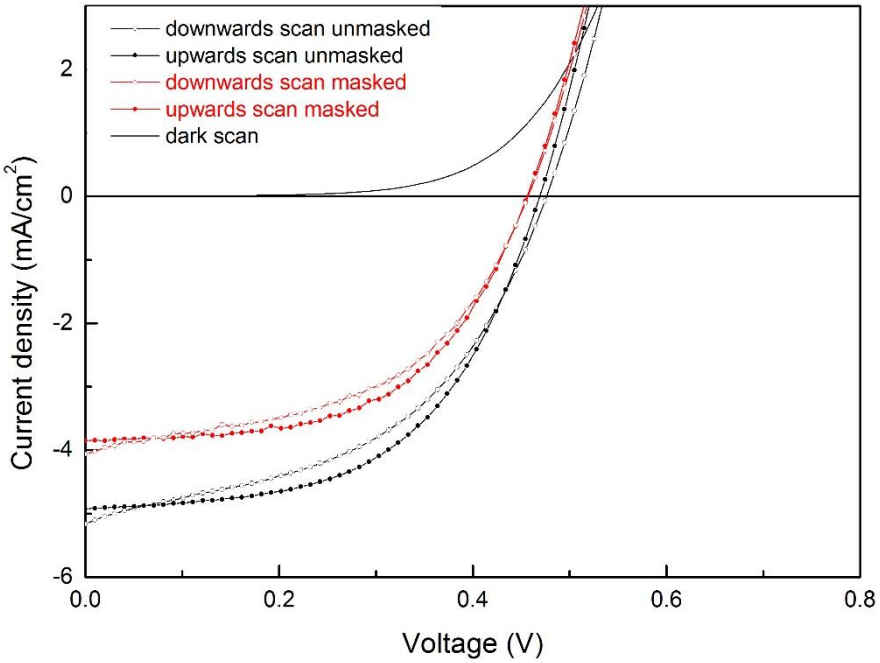

Figure 26: I/V characteristics of a solar cell masked and unmasked

Table 20: I/V values of a solar cell masked and unmasked

Sample	V_{OC} (V)	J_{SC} (mA/cm²)	FF (%)	PCE (%)
Masked	0.45	4.12	56	1.04
Unmasked	0.46	4.93	55	1.27

As depicted, the masked solar cell has a decreased J_{SC} than the unmasked whilst the other I/V characteristic data are very similar. This can be argued due to the smaller amount of photons reaching the absorber material while having the same light intensity. However, an efficiency of over 1 % for the masked solar cell was achieved, which is a tremendous success and exceeds the efficiency of current literature.

4.3. EQE measurements

Measuring the EQE of various solar cells especially for partially substituted $Rb_3Sb_2I_{9-x}Br_x$ based samples, provides interesting information about the conversion of light to electricity. Figure 27 and Figure 28 show the EQE curves of various substrates by plotting the EQE against the wavelength. The EQE curve is expected to look similar to the UV/VIS spectra when a high conversion rate of absorbed photons is given.

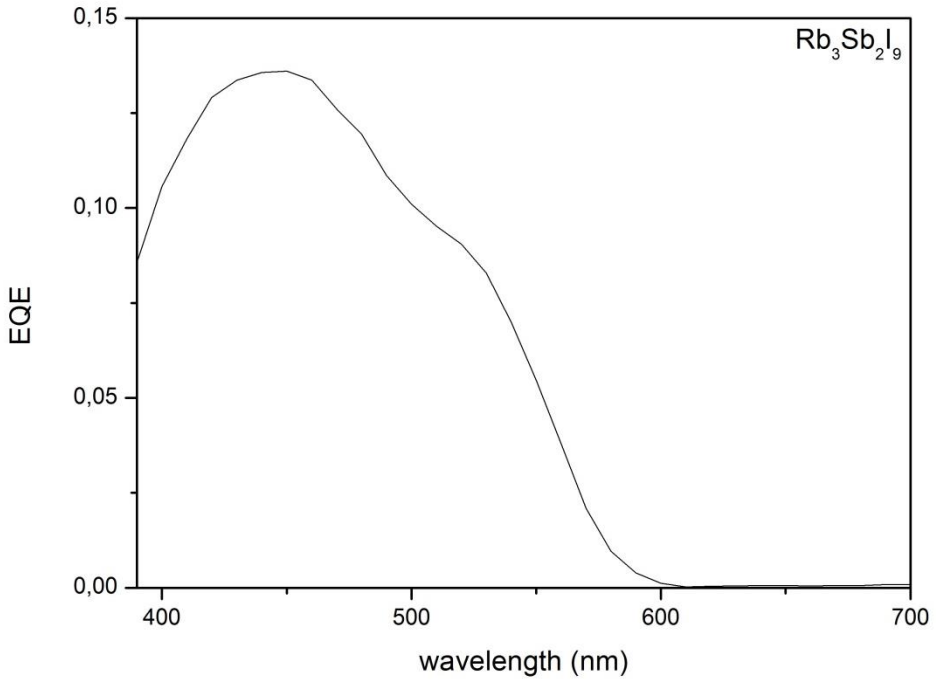

Figure 27: EQE of a solar cell using $Rb_3Sb_2I_9$ as absorber material

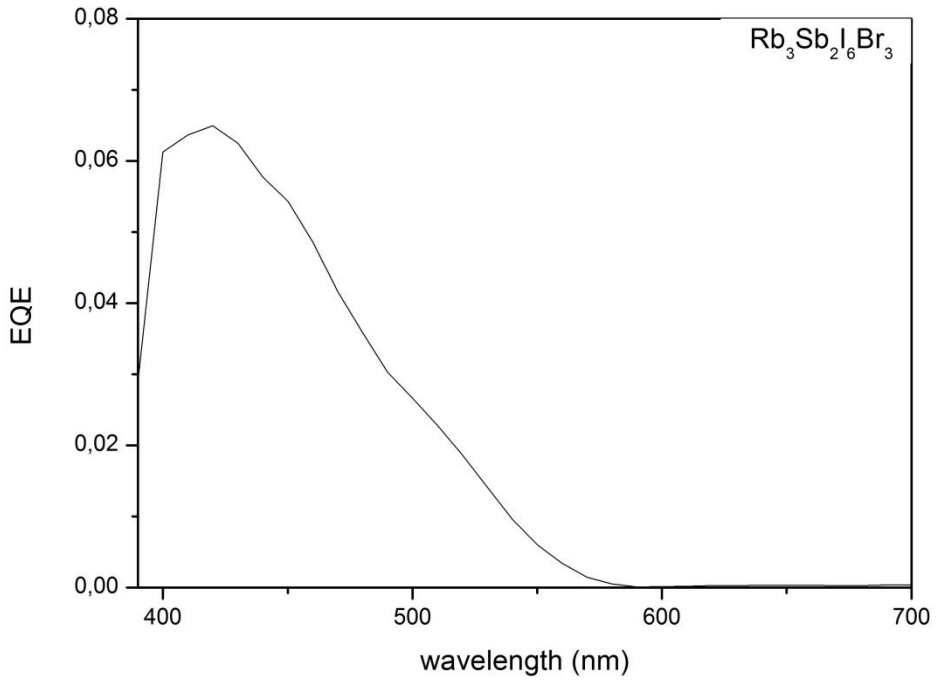

Figure 28: EQE of a solar cell using $Rb_3Sb_2I_6Br_3$ as absorber material

As seen in previous Figure 27 and Figure 28, the EQE percentage decreases by higher substitution. This is expected due to obtained lower J_{SC} in the I/V curves for higher bromide substitution. Moreover, the resulting Figure 27 and Figure 28 also show a vanishing of a shoulder at around 520 nm. By determining this shoulder in the EQE as well as in the UV/VIS means that the perovskite has a local absorption maximum at 520nm in which the material is distinct photovoltaic active. This could belong to a direct transition of an electron state to another.

Because the EQE was measured outside the glovebox and the solar cells were not encapsulated, degradation of the solar cells might occur. Therefore, the absolute numbers of the EQE cannot be compared directly. A current decrease of the cells from around 45 % was measured during only 3 minutes. This fast degradation during the EQE measurement altered the values while and before measuring. For that reason, slightly higher EQE is expected at higher wavelengths.

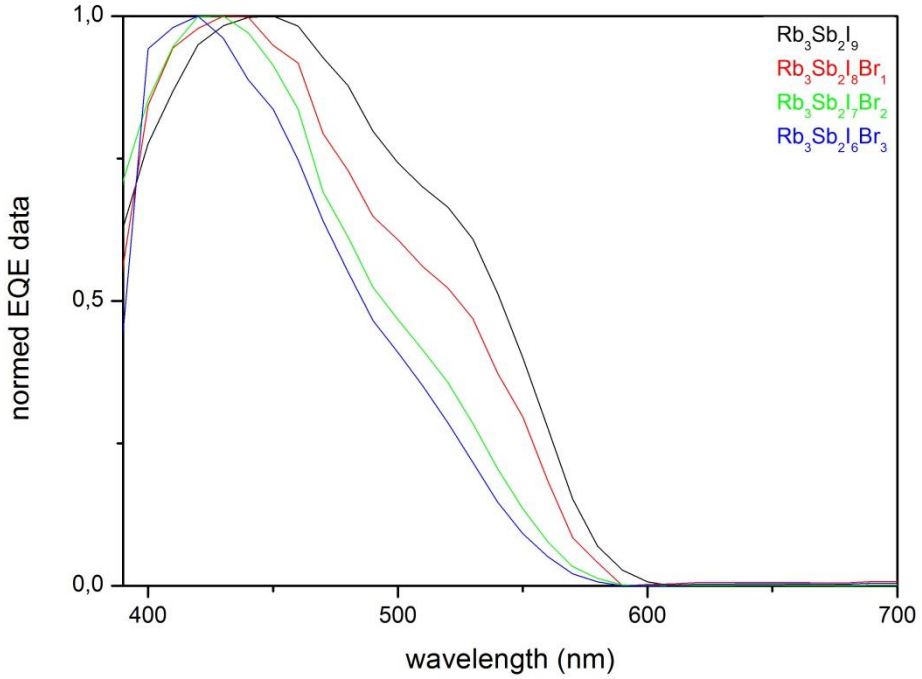

Figure 29: normalized EQE of substituted absorber material

Figure 31 shows the normed EQE of partially substituted absorber materials to demonstrate the vanishing of a local absorption peak and the shift to lower wavelengths along with higher Br-substitution.

As shown a high decrease of absorption occurs by substituting with bromide at the wavelengths between ~500 - 570 nm. Due to a lower absorption at higher wavelength, less photons are absorbed coming along with a deceased conversion which directly results in a lower J_{SC}.

The device setup for the EQE measurements were on TiO_2 and Spiro-MeOTAD with additives and a used precursor concentration of 0.2 mol/L.

5. Conclusion

The aim of this thesis was to investigate Sb-perovskites as possible alternative lead-free material in perovskite solar cells. Reasons for alternatives is the toxicity of Pb-perovskite solar cells. Using antimony in perovskite solar cells the bottleneck of Pb-perovskite solar cells would be resolved. However, the photovoltaic activity of lead-free alternatives is until now significantly lower than for lead containing ones. As the bottleneck for lead containing perovskite solar cells is its toxicity, alternative perovskite solar cells are investigated intensively to become more efficient and to compete with lead perovskite solar cells.

Several papers about a possible photovoltaic active Sb-perovskite have been published already, when this research project started; Thereunder rubidium-antimony iodide ($Rb_3Sb_2I_9$), methylammonium-antimony iodide ($MA_3Sb_2I_9$) and caesium-antimonyiodide ($Cs_3Sb_2I_9$)[8,57,58]. While the cesium-derivative possesses a good absorption spectrum with a bandgap at around 2.0 eV, a dimeric crystal structure is favored. Due to this dimeric structure, fabricated solar cells did not show any photovoltaic activity. With the MA-derivative, solar cells with a PCE of over 0.5% and a decent FF of around 55 % were achieved, whereas Rb-Sb-perovskite with a PCE of 0.66 % and a FF of 57 % were the best working Sb-perovskite solar cells by then.

The obtained data during this project shows for $MA_3Sb_2I_9$ a good absorption and a high absorption coefficient of 1×10^5 cm^{-1}. It provides a bandgap at 2.07 eV making it a promising candidate for efficient Sb-perovskite solar cells. However, literature shows a working photovoltaic device based on MA and Sb but, it was not possible to reproduce the results from literature[58]; Neither on PEDOT:PSS and $PC_{70}BM$ nor on the compact and mesoporous TiO_2 as ETL in combination with Spiro-MeOTAD as HTL.

Similar to $MA_3Sb_2I_9$, $Rb_3Sb_2I_9$ shows a high absorption in the range between 350 nm and 550nm with an absorption coefficient of 2.2×10^5 cm^{-1}. The absorber material bears a direct bandgap of 1.96 eV and an indirect at around 2.23 eV. With this bandgap wavelength below 570 nm can be absorbed and directly converted into electric energy. Table 21 shows the I/V characteristics of a solar cell from literature compared to the fabricated solar cells with spiro-MeOTAD with and without additives. Table 22 shows the device setup for the literature solar cell and the fabricated solar cells.

Table 21: I/V values of solar cells from literature, and fabricated ones on TiO_2 with and without HTL additives

	J_{SC} (mA/cm^2)	V_{OC} (V)	FF (%)	PCE (%)
Literature	2.11	0.55	57	0.66
Fabricated SC with Spiro only	1.94	0.62	41	0.49
Fabricated SC with Spiro and additives	4.01	0.51	61	1.28

Table 22: Device architecture of solar cells from literature and fabricated ones

Solar cell	Electrode	ETL	Absorber	HTL	Electrode
Literature	FTO	c-TiO_2/ m-TiO_2	$Rb_3Sb_2I_9$	Poly-TPD	Au
Fabricated with Spiro-MeOTAD	ITO	c-TiO_2/ m-TiO_2	$Rb_3Sb_2I_9$	Spiro-MeOTAD	Au

the main difference between the literature and the fabricated solar cell is the usage of a different HTL. While using only Spiro-MeOTAD result in a similar efficiency as in the literature, using additives such as LiTFSI, FK-209 and TBP enhances the charge transport and therefore increases the J_{SC}. Following Figure 30 show the I/V characteristics of the best working solar cell.

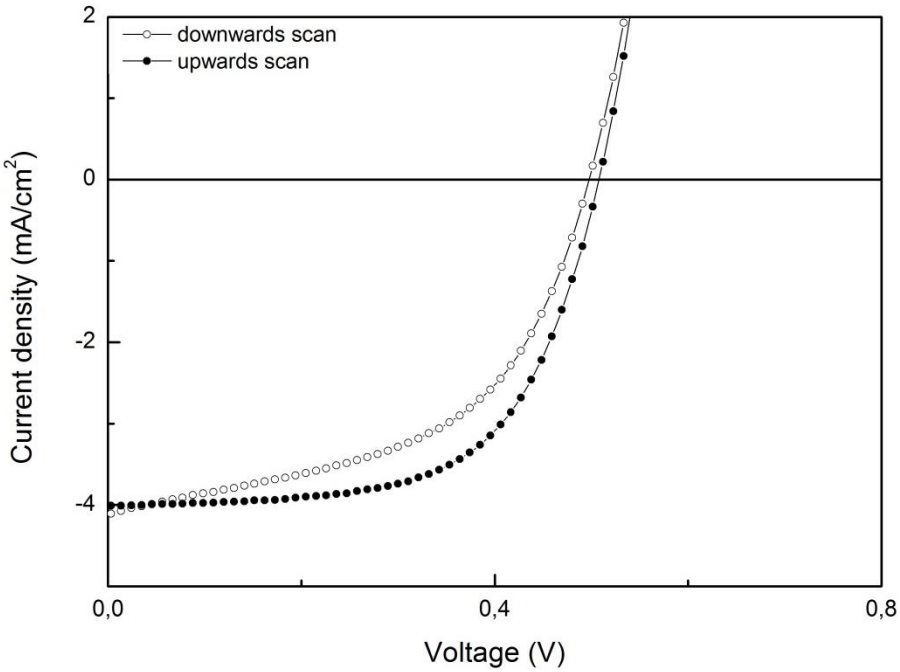

Figure 30: masked $Rb_3Sb_2I_9$ solar cell on TiO_2 and Spiro-MeOTAD with additives

Table 23: I/V values of the best masked $Rb_3Sb_2I_9$ solar cell

Sample	V_{OC} (V)	J_{SC} (mA/cm^2)	FF (%)	PCE (%)
Upwards scan	0.51	4.01	61	1.28
Downwards scan	0.50	4.11	51	1.07

A current density of up to 4 mA/cm^2 was measured and a voltage of around 0.5 V of a masked solar cell with an irradiated area of 0.0841 cm^2. It also shows a hysteresis effect scanning downwards (from 0 V to 0.8 V). This anomaly is depending on the scan direction, scan rate and scan range, the voltage conditioning history as well as the device configuration[61].

The investigation towards bromide substitution for an increased V_{OC} was a major part during this thesis. In $Rb_3Sb_2I_9$ perovskite solar cells the V_{OC} has reached up to 0.57 V with a significant high current density using TiO_2 as ETL. However, on PEDOT:PSS as HTL open circuit voltages of over 0.7 V were obtained but with a bad processability, like a rough surface, making it hard to apply the device in a planar heterojunction solar cell. The rather low V_{OC} of the solar cell in regard to the high bandgap of ~ 2.2 eV is the bottleneck for a much better device performance. Increasing the V_{OC} is fundamental for a better overall device performance even when the J_{SC} therefore would be slightly decreased. Following Figure 24 and Table 18 show the effect of bromide in the solar cell in terms of electrical device performance.

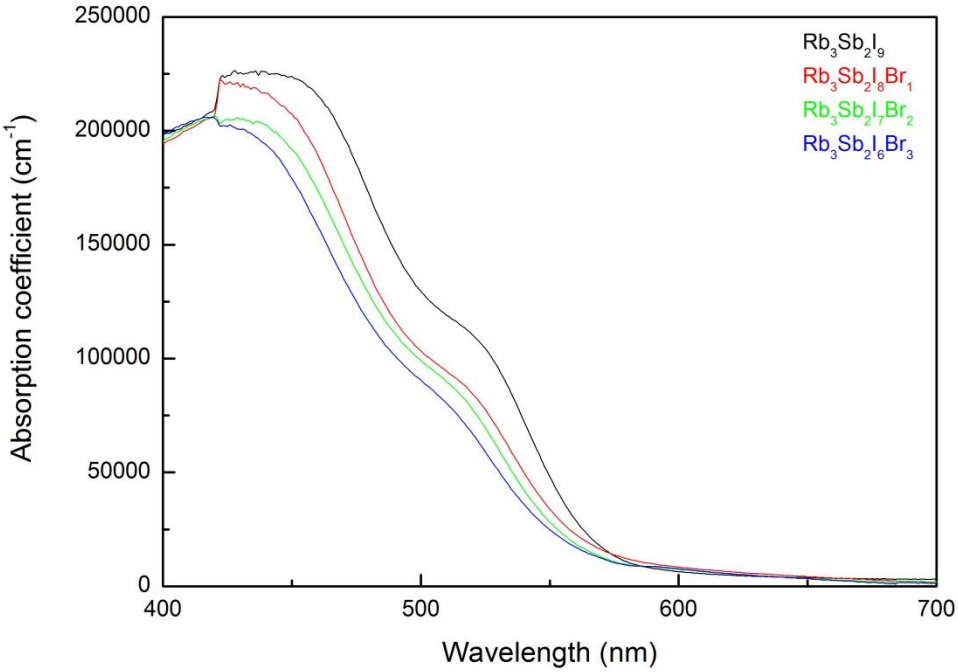

Figure 6: absorption coefficient of Rb3Sb2I9-xBrx (x = 0, 1, 2, 3) against the wavelength

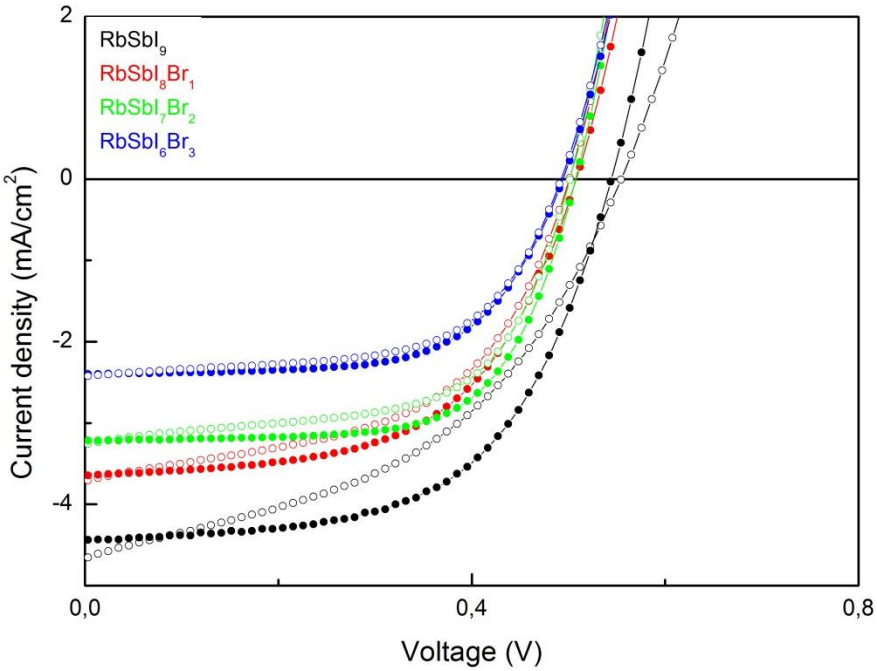

Figure 24: I/V Characteristics of solar cells using $Rb_3Sb_2I_{9-x}Br_x$ (x = 0, 1, 2, 3) as absorber materials

Table 18: Results of Rb3Sb2I9-xBrx (x =0, 1, 2, 3)

Sample	V_{OC} (V)	J_{SC} (mA/cm^2)	FF (%)	PCE (%)
$Rb_3Sb_2I_9$	**0.54**	**4.4**	**58**	**1.40**
$Rb_3Sb_2I_8Br$	**0.51**	**3.6**	**56**	**1.03**
$Rb_3Sb_2I_7Br_2$	**0.51**	**3.2**	**66**	**1.08**
$Rb_3Sb_2I_6Br_3$	**0.49**	**2.4**	**64**	**0.74**

A decrease of the short circuit current density as expected is very distinct by increased bromide substitution, while a decrease of the open circuit voltage appears simultaneously.

Investigation of what causes the decrease of the V_{OC} lead to the Urbach energy, to determine the structural disorder, the amount of impurities and amount of deep trap effects. An increase of the Urbach energy by higher bromide substitution was found. While the Urbach energy for the pure iodide perovskite ($Rb_3Sb_2I_9$) was at around 79 meV (literature around 90 meV[8]), for the $Rb_3Sb_2I_6Br_3$ material an Urbach energy of 126 meV was determined. The decrease of the V_{OC} by increased substitution is therefore a product of a higher disorder in the perovskite.

Summarizing all the received data during this thesis and from the literature, Sb-perovskite solar cells have their disadvantages up to now concerning the overall device performance in regard to other perovskite solar cells. However, an increase of PCE and a doubling of the J_{SC} compared to existing Sb-perovskite solar cells at the beginning of this thesis was achieved. This is a big step forward making them more interesting alike other lead-free alternative perovskite solar cell devices. Having rubidium as an A cation makes the system not only more efficient but furthermore also easier in terms of processability providing smooth surfaces and a good adhesion when spin coating. Calculations of $Rb_3Sb_2I_9$ show a theoretical current density of around 10 mA/cm^2, providing enough room for further improvement of device performance[8].

Even though a high bandgap for the Rb-perovskite of 2.24 eV was found the V_{OC} is rather low. Attempts to increase the open circuit voltage were made by substitution of the iodide anion with bromide to enhance the voltage. However, results show a decrease of the V_{OC} due to an increased Urbach energy. Using a different HTL and ETL material might provide such a positive effect.

Characterizing the absorber material and optimizing the device setup as well as using another device setup to enhance the photodiodic properties was a huge progress and success to make Sb-based solar cells more interesting; especially for further investigation of $Rb_3Sb_2I_9$ as absorber layer in photovoltaic devices.

6. List of Figures

7. List of Equations:

8. List of tables

9. Literature

1) https://www.eia.gov/outlooks/ieo/world.php (accessed 7.28.17)

2) https://yearbook.enerdata.net/total-energy/world-energy-production.html (accessed 7.28.17)

3) Fik Meijer. A History of Seafaring in the Classical World. Croom Helm.Ltd. **2014**

4) Soteris Kalogirou. “processes and systems.” Solar energy engineering, Elsevier, second edition, **2014**

5) Soteris Kalogirou. ”photovoltaic systems.” Solar energy engineering, Elsevier, second edition, **2014**

6) Holleman Wiberg. Lehrbuch Der Anorganischen Chemie, de Gruyter, 102 nd edition, **2007**

7) Saunders BR, Turner ML. Nanoparticle-polymer photovoltaic cells. Adv Colloid Interface Sci. **2008**, 28,138, 1-23

8) Harikesh, P. et al. Rb as an Alternative Cation for Templating Inorganic Lead-Free Perovskites for Solution Processed Photovoltaics, Chem. Mater. **2016**, 28, 7496 -7504

9) Scharber MC, Mühlbacher D, Koppe M, et al. Design Rules for Donors in Bulk Heterojunction Solar Cells Towards 10 % Energy-Conversion Efficiency. Adv Mater. **2006**, 18, 789-794.

10) Günes S, Sariciftci NS. Hybrid solar cells. Inorganica Chim Acta. **2008**; 361, 581-588.

11) Mertens K. Photovoltaik Lehrbuch Zu Grundlagen, Technologie Und Praxis. Carl Hanser Verlag GmbH & Co. KG; 2nd Edition, **2013**, 298

12) Xuanzhi Wu. High-efficiency polycrystalline CdTe thin-film solar cells. Solar energy, **2004**, 77, 803-814

13) M.A.Islam, K.S.Rahman. Fabrication of high efficiency sputtered CdS:O/CdTe thin film solar cells from window/absorber layer growth optimization in magnetron sputtering. Solar Energy Mat. And Solar Cells, **2017**, 172, 384-393

14) P. Jackson, R. Wuerz, D. Hariskos, E. Lotter, W. Witte, M. Powalla**:** Effects of heavy alkali elements in Cu(In,Ga)Se2 solar cells with efficiencies up to 22.6%. Phys. Status Solidi RRL, **2016**, 10, 583-586

15) A. Yella, H.W. Lee, H. et al. Porphyrin-sensitized solar cells with cobalt (II/III)-based redox electrolyte exceed 12 percent efficiency. Science. **2011,** 334, 629-634

16) Hara, Kohjiro; Arakawa, Hironori. "Chapter 15. Dye-Sensitized Solar Cells" Handbook of Photovoltaic Science and Engineering. John Wiley & sons. **2005**

17) A. Kojima, K. Teshima, Y. Shirai, T. Miyasaka, *J. Am. Chem. Soc.* **2009**, 131, 6050-6051

18) S. Hoefler, Trimmel G., Rath T. Progress on lead-free metal halide perovskites for photovoltaic apllications: a review. Monatsh Chem. **2017**, 148, 795-826

19) Y. Liu, Z. Yang, D. Cui, et al.. Two- Inch-Sized Perovskite CH3NH3PbX3 (X = Cl, Br, I) Crystals: Growth and Characterization. Adv. Mater., **2015**, 27, 5176-5183

20) Y. Yu, P. Gao, Development of electron and hole selective contact materials for perovskite solar cells, Chin. Chem. Lett. **2017**, 28, 1144-1152

21) J.-P. Correa-Baena, A. Abate, M. The rapid evolution of highly efficient perovskite solar cells. *Energy Environ. Sci.*; **2017,** 10, 710-727

22) I. J. Ogundana and S. Y. Foo, Improving the Morphology of the Perovskite Absorber Layer in Hybrid Organic/Inorganic Halide Perovskite MAPbI3 Solar Cells, Journal of Solar Energy, **2017**, doi:10.1155/2017/8549847

23) J. Liu, G. Wang, Understanding the Role of the Electron-Transport Layer in Highly Efficient Planar Perovskite Solar Cells., Chem. Phys. Chem **2017**, 18, 617-625

24) NREL. Best Research-Cell Efficiencies. http://www.nrel.gov/ncpv/images/efficiency_chart.jpg (accessed 24/6/2017).

25) Brandt, R. E.; Stevanović, V.; Ginley, D. S.; Buonassisi, T. Identifying defect-tolerant semiconductors with high minority-carrier lifetimes: beyond hybrid lead halide perovskites. MRS Commun. **2015**, 5, 265−275.

26) Xing, G.; Mathews, N.; Sun, S.; Lim, S. S.; Lam, Y. M.; Grätzel, M.; Mhaisalkar, S.; Sum, T. C. Long-Range Balanced Electron- and Hole-Transport Lengths in Organic-Inorganic CH3NH3PbI3. Science, **2013**, 342, 344−347.

27) Li, Z.; Kulkarni, S. A.; Boix, P. P.; Shi, E.; Cao, A.; Fu, K.; Batabyal, S. K.; Zhang, J.; Xiong, Q.; Wong, L. H.; Mathews, N.; Mhaisalkar, S. G. Laminated Carbon Nanotube Networks for Metal Electrode-Free Efficient Perovskite Solar Cells. ACS Nano **2014**, 8, 6797−6804.

28) Docampo, P.; Ball, J. M.; Darwich, M.; Eperon, G. E.; Snaith, H. J. Efficient organometal trihalide perovskite planar-heterojunction solar cells on flexible polymer substrates. Nat. Commun, **2013**, 4, 2761.

29) Mei, A.; Li, X.; Liu, L.; Ku, Z.; Liu, T.; Rong, Y.; Xu, M.; Hu, M.; Chen, J.; Yang, Y.; Grätzel, M.; Han, H. A hole-conductor−free, fully printable mesoscopic perovskite solar cell with high stability. Science, **2014**, 345, 295−298.

30) Burschka, J.; Pellet, N.; Moon, S.-J.; Humphry-Baker, R.; Gao, P.; Nazeeruddin, M. K.; Gratzel, M. Sequential deposition as a route to high-performance perovskite-sensitized solar cells. Nature, **2013**, 499, 316−319.

31) Jeon, N. J.; Noh, J. H.; Kim, Y. C.; Yang, W. S.; Ryu, S.; Seok, S. I. Solvent engineering for high-performance inorganic−organic hybrid perovskite solar cells. Nat. Mater., **2014**, 13, 897−903.

32) Nie, W.; Tsai, H.; Asadpour, R.; Blancon, J.-C.; Neukirch, A. J.; Gupta, G.; Crochet, J. J.; Chhowalla, M.; Tretiak, S.; Alam, M. A.; Wang, H.-L.; Mohite, A. D. High-efficiency solution-processed perovskite solar cells with millimeter-scale grains. Science, **2015**, 347, 522−525.

33) McMeekin, D. P.; Sadoughi, G.; Rehman, W.; Eperon, G. E.; Saliba, M.; Hörantner, M. T.; Haghighirad, A.; Sakai, N.; Korte, L.; Rech, B.; Johnston, M. B.; Herz, L. M.; Snaith, H. J. A mixed-cation lead mixed-halide perovskite absorber for tandem solar cells. Science, **2016**, 351, 151−155.

34) Sutton, R. J.; Eperon, G. E.; Miranda, L.; Parrott, E. S.; Kamino, B. A.; Patel, J. B.; Hörantner, M. T.; Johnston, M. B.; Haghighirad, A. A.; Moore, D. T.; Snaith, H. J. Bandgap-Tunable Cesium Lead Halide Perovskites with High Thermal Stability for Efficient Solar Cells. Adv. Energy Mater. **2016**, 6, 1502458

35) Jeon, N. J.; Noh, J. H.; Yang, W. S.; Kim, Y. C.; Ryu, S.; Seo, J.; Seok, S. I. Compositional engineering of perovskite materials for high performance solar cells. Nature, **2015**, 517, 476−480.

36) T. J. Jacobsson, J.-P. Correa-Baena, M. Pazoki, M. Saliba, K. Schenk, M. Grätzel, A. Hagfeldt; Energy Environ*. Sci.*, **2016,** 9, 1706-1724

37) M. Saliba, T. Matsui, K. Domanski, J.-Y. Seo, A. Ummadisingu, S. M. Zakeeruddin, J.-P. Correa-Baena, W. R. Tress, A. Abate, A. Hagfeldt, M. Grätzel. Exploration of the compositional space for mixed lead halogen perovskites for high efficiency solar cells. *Science*, 2016, 354, 206-209

38) Yin, W.-J.; Shi, T.; Yan, Y. Unique Properties of Halide Perovskites as Possible Origins of the Superior Solar Cell Performance. Adv. Mater. **2014**, 26, 4653−4658.

39) Yin, W.-J.; Shi, T.; Yan, Y. Superior Photovoltaic Properties of Lead Halide Perovskites: Insights from First-Principles Theory. J. Phys. Chem. C, **2015**, 119, 5253−5264.

40) Leijtens, T.; Eperon, G. E.; Pathak, S.; Abate, A.; Lee, M. M.; Snaith, H. J. Overcoming Ultraviolet Light Instability of Sensitized TiO2 with Meso-

Superstructured Organometal Tri-Halide Perovskite Solar Cells. Nat. Commun., **2013**, 4, 2885−2893.

41) Noh, J. H.; Im, S. H.; Heo, J. H.; Mandal, T. N.; Seok, S. I. Chemical Management for Colorful, Efficient, and Stable Inorganic Organic Hybrid Nanostructured Solar Cells. Nano Lett., **2013**, 13, 1764−1769.

42) Christians, J. A.; Herrera, P. A. M.; Kamat, P. V. Transformation of the Excited State and Photovoltaic Efficiency of CH3NH3PbI3 Perovskite upon Controlled Exposure to Humidified Air. J. Am. Chem. Soc., **2015**, 137, 1530−1538.

43) Chen Q, De Marco N, Yang Y, Song T-B, Chen C-C, Zhao H, Hong Z, Zhou H, Yang Y. Under the spotlight: The organic–inorganic hybrid halide perovskite for optoelectronic applications. Nano Today, 2015, 10, 355-396

44) Borriello I, Cantele G, Ninno. Combined experimental and theoretical investigation of optical, structural, and electronic properties of CH3NH3SnX3 thin films (X=Cl,Br), Phys. Rev. B 77., 2008, 0451291-0451296

45) Maughan AE, Kurzman JA, Neilson JR. Hybrid Inorganic–Organic Materials with an Optoelectronically Active Aromatic Cation: (C7H7)2SnI6 and C7H7PbI3. Inorg Chem., **2015**, 54, 370-378

46) Ziran Zhao, F. Gu. Mixed-Organic-Cation Tin Iodide for Lead-Free Perovskite Solar Cells with an Efficiency of 8.12 %. Adv. Sci., **2017**, 1700204, https://doi.org/10.1002/advs.384

47) Noel NK, Stranks SD, Abate A, Wehrenfennig C. et al.. Lead-free organic–inorganic tin halide perovskites for photovoltaic applications. Energy Environ Sci. 2014, 7, 3061-3068

48) Takahashi Y, Obara R, Lin Z-Z, Takahashi Y, Naito T, Inabe T, Ishibashi S, Terakura K. Charge-transport in tin-iodide perovskite CH3NH3SnI3: origin of high conductivity. Dalton Trans., **2011**, 40, 5563-5568

49) Lee B, Stoumpos CC, Zhou N, Hao F, Malliakas C, Yeh C-Y,Marks TJ, Kanatzidis MG, Chang RPH J. Air-stable molecular semiconducting iodosalts for solar cell applications: Cs2SnI6 as a hole conductor.Am Chem Soc, **2014**, 136,15379 -15385

50) Shannon RD. Revised effective ionic radii and systematic studies of interatomic distances in halides and chalcogenides Acta Crystallogr, **1976**, 32, 751- 767

51) Lehner AJ, Fabini DH, Evans HA, He´bert CA, Smock SR, Hu J, Wang H, Zwanziger JW, Chabinyc ML, Seshadri R. Crystal and Electronic Structures of Complex Bismuth Iodides A3Bi2I9 (A = K, Rb, Cs) Related to Perovskite: Aiding the Rational Design of Photovoltaics Chem Mater. **2015,** 27, 7137-7148

52) Park B-W, Philippe B, Zhang X, Rensmo H, Boschloo G,Johansson EMJ. Bismuth Based Hybrid Perovskites A3Bi2 I9 (A: Methylammonium or Cesium) for Solar Cell Application. Adv Mater, **2015,** 27,6806-6813

53) Kamminga ME, Stroppa A, Picozzi S, Chislov M, Zvereva IA, Baas J, Meetsma A, Blake GR, Palstra TTM. Polar Nature of (CH3NH3)3Bi2I9 Perovskite-Like Hybrids. Inorg Chem, **2017,** 56, 33-41

54) Zheng Zhang, X. Li. High-Quality (CH3NH3)3Bi2I9Film-Based Solar Cells: Pushing Efficiency up to 1.64 %. J. of Phys. Chem. Lett. **2017**, 8, 4300-4307

55) Öz S, Hebig J-C, Jung E, Singh T, Lepcha A, Olthof S, Flohre J, Gao Y, German R, van Loosdrecht PHM, Meerholz K, Kirchartz T, Mathur. Zero-dimensional (CH3NH3)3Bi2I9 perovskite for optoelectronic applications. Solar Energy Mater. Solar Cells, **2016**, 158, 195-201

56) Slavney, A. H.; Hu, T.; Lindenberg, A. M.; Karunadasa, H. I. A Bismuth-Halide Double Perovskite with Long Carrier Recombination Lifetime for Photovoltaic Applications. J. Am. Chem. Soc. **2016**, 138, 2138−2141.

57) Saparov, B.; Hong, F.; Sun, J.-P.; Duan, H.-S.; Meng, W.; Cameron, S.; Hill, I. G.; Yan, Y.; Mitzi, D. B. Thin-Film Preparation and Characterization of

Cs3Sb2I9: A Lead-Free Layered Perovskite Semiconductor. Chem. Mater. **2015**, 27, 5622−5632.

58) Hebig, J.-C.; Kühn, I.; Flohre, J.; Kirchartz, T. Optoelectronic Properties of (CH3NH3)3Sb2I9 Thin Films for Photovoltaic Applications. ACS Energy Lett. **2016**, 1, 309−314.

59) Mitzi, D. B.; Brock, P. Structure and Optical Properties of Several Organic−Inorganic Hybrids Containing Corner-Sharing Chains of Bismuth Iodide Octahedra. Inorg. Chem. **2001**, 40, 2096− 2104.

60) Yin, W.-J.; Shi, T.; Yan, Y. Unusual defect physics in CH3NH3PbI3 perovskite solar cell absorber. Appl. Phys. Lett. **2014**, 104, 063903 https://doi.org/10.1063/1.4864778

61) Bo Chen. J. Origin of J–V Hysteresis in Perovskite Solar Cells. *Phys. Chem. Lett.*, **2016**,7, 905–917